Mohn-Sverdrup Center,

Nansen Environmental and Remote Sensing Center

A non-profit environmental research center affiliated with the University of Bergen

Thormøhlensgate 47
N-5006 Bergen, Norway
Tel: +47 55 20 58 00
Fax: +47 55 20 58 01

Technical Report No. 304

A multi-category sea-ice model

by

Knut A. Lisæter

April 2009

Nansen Environmental and Remote Sensing Center (NERSC)
Thormøhlensgate 47
N-5006 Bergen
Norway

phone +47 55205800
fax +47 55205801
email adm@nersc.no

TITLE	**REPORT IDENTIFICATION**
A multi-category sea-ice model	NERSC Technical report no. 304
CLIENT	**CONTRACT NO.**
CLIENT	CONTRACT
CLIENT REFERENCE	**AVAILABILITY**
- -	OPEN
INVESTIGATOR	**AUTHORIZATION**
Knut Arild Lisæter email: Knut.Liseter@nersc.no	Bergen, April 14, 2009 Prof. Ola M. Johannessen Director NERSC

Contents

Abstract

The framework for a multi-category sea-ice model is presented. The ice model describes the ice thickness distribution by using a set of delta-functions, where each delta-function has an associated fractional coverage c_i and ice thickness h_i. The formulation of ice ridging and rafting is given, building on the theory of Thorndike et al. (1975). The thermodynamic formulation is also given, with emphasis on how the model treats the heat conduction in the ice. The formulation is extended by introducing the concept of ice classes. The ice classes are constraints put on the description of the ice thickness distribution, whose purpose is to give a practical formulation of the ice thickness distribution. A demonstration of the ice model performance is given, where the model is coupled to the HYCOM ocean model and the EVP sea-ice rheology. It is shown how the ice model is able to reproduce the main features of the Arctic ice cover as well as the transport of sea ice out of the Fram Strait.

1 Introduction

Sea ice is an important component of the climate system. Its presence in the Arctic and Antarctic has a strong impact on the fluxes of momentum, moisture and heat from the ocean to the atmosphere. The strong impact of sea ice is perhaps best demonstrated in the way it affects the heat fluxes. In the Arctic it is not uncommon to have heat fluxes close to a kilowatt between the ocean and atmosphere when ice is absent. The presence of ice, on the other hand, can reduce this flux by two orders of magnitude (Maykut and Untersteiner, 1971). Although the presence/absence of ice is perhaps the most important effect when it comes to insulating the ocean from the atmosphere, the thickness of ice is important as well. The thicker the ice is, the stronger will its insulating effect be.

The most common model formulations use a simple two-category ice thickness formulation, where the grid cell is divided into a fraction with open water, and a remaining fraction consisting of ice of thickness h_i. This formulation has proven to give good results, but it misses some important properties of the ice cover. For instance, lateral melt parameterizations are needed to account for the melting of ice floe edges, although this effect is not that important for very large ice floes (Steele, 1992). Perhaps more importantly, lateral melt parameterizations are needed to account for thinner ice melting quicker than thick ice (Häkkinen and Mellor, 1992). Such parameterizations can have a strong effect on the seasonal variations of the ice cover, and associated ocean-atmosphere heat exchange (Mellor and Kantha, 1989; Harvey, 1990). Sea ice models which describe the ice thickness distribution should not need such parameterizations if the thin ice is sufficiently resolved by the model.

In this work we present the development of a thermodynamic-kinematic sea ice model and its implementation as an ice model component coupled to the HYCOM ocean model (Bleck, 2002) and the Elastic-Viscous-Plastic sea ice rheology model of Hunke and Dukowicz (1997). The thermodynamic part of the model calculate the sea ice growth as well as the cooling and heating rates of the ocean. In effect, it replaces the surface flux calculations used in HYCOM, which has a simple treatment of sea ice at the moment of writing. The kinematic part of the sea ice model describes the changes to the ice thickness distribution as sea ice is ridged and rafted. For instance, during continued convergence of sea ice, so called pressure ridges are formed. As a result of this the thickness distribution changes as thinner ice gets piled up and forms thicker ice.

The model uses the theory of Thorndike et al. (1975) to describe the sea ice thickness distribution, and the implementation gives the ice thickness distribution as a set of discrete ice thicknesses with a fractional coverage of the sea surface. In mathematical terms, the ice thickness distribution is described as a sum of delta functions $c_i\delta(h - h_i)$ where c_i is the fractional ice coverage and h_i is the ice thickness occupying this fraction.

Models with similar ideas for modeling the ice thickness distribution already exist (Salas Mélia, 2002; Bitz et al., 2001). Here, we focus on the design choices done for our model, and on the specification of model thermodynamics and the ice thickness distribution. Section 2 deals with the thermodynamic treatment in the model. Section 3 describes the ice thickness distribution description, continued in Section 4 which further discusses the implementation, and how the ice thickness distribution is managed for practical purposes. Results from an implementation with the HYCOM ocean model and the EVP rheology is presented in Section 5, and the work is summarized in Section 8.

2 Thermodynamic model

This section presents the treatment of the heat fluxes, and the resulting ocean temperature change and ice freezing/melting rates. The different atmospheric and oceanic heat fluxes acting on the ice are based on well-known parameterizations, and their forms are given in Appendix A.

The main focus of this section is on the conductive heat flux formulation acting in the ice, and how this is treated in two different cases, Section 2.1. The two cases are defined by a user-set ice thickness, h_L. In the first case, $(h < h_L)$ the ice has a linear temperature profile, and an additional

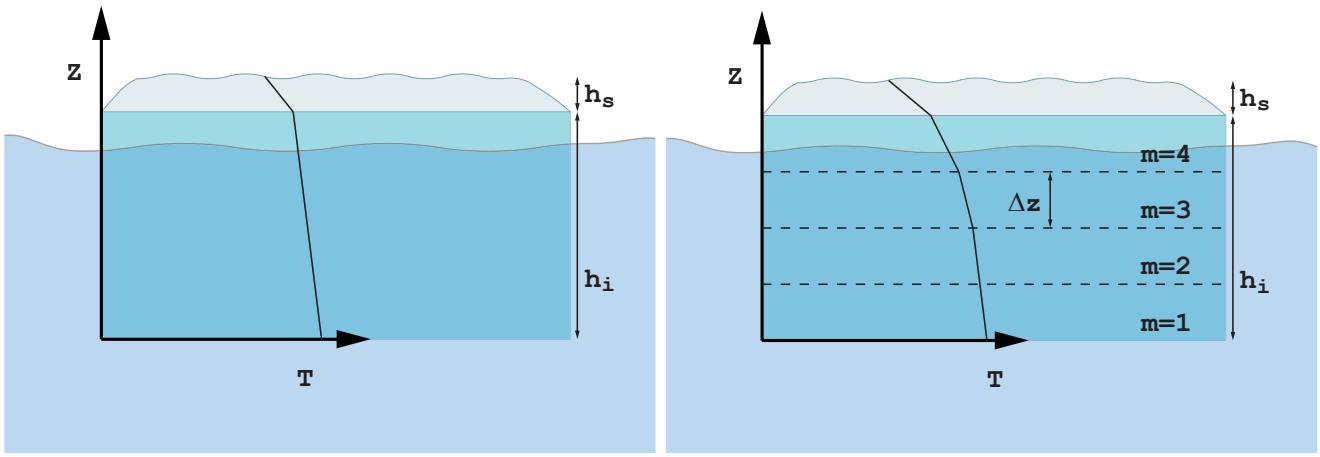

(a) Thin ice ($h_i \leq h_L$) (b) Thick ice ($h_i > h_L$)

Figure 1: Illustrations of vertical temperature distribution in the ice for a case with thin ice and for a case with thick ice

parameterization is used to account for the specific heat of the ice slab. The second case is for ice of thickness greater than h_L, in this case the heat equation is solved in the ice slab using a finite difference scheme.

We also present the surface heat budget of the model, in Section 2.2, which utilizes all the parameterizations of heat fluxes described in Appendix A and in Section 2.1. Although the complete model describes the ice thickness distribution, this concept is not needed at this stage, for that we refer to Sections 3 and 4. The equations given in this section therefore refer to an ice slab of thickness h_i and snow thickness h_s.

2.1 Heat conduction fluxes in the ice

In this section the heat fluxes occurring within the ice due to heat conduction and thermal inertia are described. The vertical conduction of heat in ice and snow is given as

$$c_{\mathrm{p\{i,s\}}}\rho_{\mathrm{i,s}}\frac{\partial T_{\mathrm{i,s}}}{\partial t} = k_{\mathrm{i,s}}\frac{\partial^2 T_{i,s}}{\partial z^2}\,, \tag{1}$$

where $c_{\mathrm{p\{i,s\}}}$ is the specific heat capacity, $\rho_{i,s}$ is the density, and $k_{i,s}$ is the heat conductivity of snow (s) or ice (i) all assumed constant in each material. Due to numerical constraints, Equation (1) is solved differently depending on whether the ice is thick or thin. Thick or thin ice is determined by a limit h_L, and the vertical discretization and temperature distribution in the ice is illustrated in Figure 1 for the two different cases. The approaches used will be discussed next.

2.1.1 Thin ice

Numerical considerations prevent us from solving the heat equation when the ice thickness is small. This ice is therefore treated by parameterizations which makes sure the energy budget is closed. The bulk temperature of the entire ice slab is given as

$$T_{\mathrm{i,blk}} = \frac{1}{h_i}\int_0^{h_i} T_i \mathrm{d}z, \tag{2}$$

where the z-coordinate system is given in Figure 1(a). The stationary solution of Equation (1) is

$$\frac{\partial^2 T_{i,s}}{\partial z^2} = 0 \Longrightarrow T_{\mathrm{i,s}} = a_{\mathrm{i,s}} z + b_{\mathrm{i,s}}\,, \tag{3}$$

which is used to describe the temperature profile in the snow (s) and in the ice (i).

The condition at the bottom of the ice slab ($z = 0$) is that the temperature is at the freezing point of seawater, $T_i(0) = T_f(S_w)$. The conductive heat flux is calculated using an effective heat conductivity for the combined ice/snow system. The individual temperature profiles in the snow and ice are linear, Equation (3), and they result in the same flux because flux balance at the ice/snow interface is imposed. The relationship between the effective heat flux and the heat fluxes in the ice and snow is

$$F_c = -k_{\text{eff}} \frac{\Delta T_i + \Delta T_s}{h_i + h_s} = -k_i \frac{\Delta T_i}{h_i} = -k_s \frac{\Delta T_s}{h_s}\,, \tag{4}$$

where ΔT_i and ΔT_s are the temperature differences across the ice(i) and snow(s) layers. By using Equation (4) the effective heat conductivity becomes

$$k_{\text{eff}} = \frac{(h_i + h_s) k_s k_i}{h_i k_s + h_s k_i}\,. \tag{5}$$

The conductive heat flux for thin ice gives the same value for both the bottom and top of the ice slab

$$F_c^{\text{bot}} = F_c^{\text{top}} = F_c\,. \tag{6}$$

In addition to the conductive heat flux, a simple parameterization of ice heating is used for thin ice. As the surface temperature of the ice is changing, some of the heat flux going into the ice will change the temperature of the ice. This effect is present as a heat flux at the top of the ice/snow system. The specific heat budget is only solved for ice, the snow is treated as having zero heat capacity. Using Equations (2) and (3), the bulk temperature of the ice slab can be related to the temperature difference across the ice slab,

$$\Delta T_i = T_i(h_i) - T_i(0) = T_i(h_i) - T_f(S_w) = 2(T_{\text{i,blk}} - T_f(S_w))\,. \tag{7}$$

For a given change in surface temperature T_{srf} there will be an associated change in bulk temperature $T_{\text{i,blk}}$ of the ice. Since $\Delta T_i + \Delta T_s = T_{\text{srf}} - T_f(S_w)$, Equations (4), and (7) give

$$T_{\text{i,blk}} = \frac{T_{\text{srf}} k_s h_i + T_f(S_w)\,(2k_i h_s + k_s h_i)}{2\,(k_s h_i + k_i h_s)}\,. \tag{8}$$

The heat required to increase the internal energy of the ice is then related to the change of surface temperature. This heat flux is applied at the top surface

$$F_{\text{inrt}} = -c_{\text{pi}} \rho_i h_i \frac{\partial T_{\text{i},blk}}{\partial t} = -c_{\text{pi}} \rho_i h_i \frac{k_s h_i}{2\,(k_s h_i + k_i h_s)} \frac{\partial T_{\text{srf}}}{\partial t}\,. \tag{9}$$

One of the benefits of using this simple parameterization is that a smooth evolution of the surface temperature is ensured. In absence of the flux F_{inrt}, discontinuities of the atmospheric forcing can lead to discontinuous surface temperatures.

2.1.2 Thick ice

When the ice is thicker than the limiting thickness h_L, a numerical solver of Equation (1) is used. The energy budget is only calculated for ice in this procedure, the snow is, as in the case with thin ice, treated as having zero heat capacity. The internal ice temperatures are calculated by using a forward–in–time, central–in–space discretization. It is given as

$$T_{\text{i,m}}^{n+1} = T_{\text{i,m}}^{n} - \frac{\Delta t}{\rho_i c_{\text{pi}} (\Delta z)} \left(F^{\star}_{\text{c,m}+1/2} - F^{\star}_{\text{c,m}-1/2} \right) \tag{10}$$

where $T^n_{\mathrm{i,m}}$ is the bulk temperature of ice layer m at time step n. The grid spacing in the vertical is $\Delta z = h_i/N$ where N is the number of layers in the vertical, see Figure 1(b) for an illustration of the temperature discretization.

The temporal time step is Δt, while the flux between layers $F^\star_{\mathrm{c,m+1/2}}$ is set as

$$F^\star_{\mathrm{c,m+1/2}} = -k_i \frac{T^n_{\mathrm{i,m+1}} - T^n_{\mathrm{i,m}}}{\Delta z} \qquad m \in \{1, ..., N-1\} \tag{11}$$

The boundary conditions $F^\star_{\mathrm{c,N+1/2}}$ and $F^\star_{\mathrm{c,1/2}}$ need to be specified in addition to (11). At the lowest layer ($m = 1$) the flux $F^\star_{c,1/2}$ is specified in terms of the temperature at the bottom of the ice, and the distance between the bottom and the lowest layer center

$$F^{\mathrm{bot}}_c = F^\star_{\mathrm{c,1/2}} = -k_i \frac{T^n_{\mathrm{i,1}} - T_f}{\frac{\Delta z}{2}} \,. \tag{12}$$

At the top of the ice slab, two heat flux parameterizations are used. The ice heating parameterization F_{inrt} is used when calculating the surface heat balance, as for thin ice. The approach is similar to the one used in the case with thin ice, but it is only used for the top half of the uppermost layer in the ice. Based on Equation (9), we obtain

$$F_{\mathrm{inrt}} = -c_{\mathrm{pi}}\rho_i \frac{h_i}{2N} \frac{k_s \frac{h_i}{2N}}{2\left(k_s \frac{h_i}{2N} + k_i h_s\right)} \frac{\partial T_{\mathrm{srf}}}{\partial t} \,. \tag{13}$$

At the top of the ice/snow slab ($m = N$) the surface temperature and the effective heat conductivity across the snow and half of the uppermost ice layer is used to calculate the conductive heat flux;

$$F^{\mathrm{top}}_c = -\,k_{\mathrm{eff}} \frac{T_{\mathrm{srf}} - T^n_{\mathrm{i,N}}}{h_s + \frac{h_i}{2N}} \qquad k_{\mathrm{eff}} = \frac{(\frac{h_i}{2N} + h_s)k_s k_i}{\frac{h_i}{2N}k_s + h_s k_i} \,, \tag{14}$$

where k_{eff} has been calculated by similar method to that in the case with thin ice, Equation (5). The only difference is that in the thin ice case, the ice bottom surface was used as the lower interface for the conductive heat flux, whereas the midpoint of the top layer is used in the case with thick ice.

The ice heating parameterization F_{inrt} is used to compensate for low spatial resolution in the surface ice layer. In the limit as the number of layers $N \to \infty$ it is easily seen that $F_{\mathrm{inrt}} \to 0$ while the conductive heat flux F^{top}_c may converge to a nonzero value.

The total heat flux going into the ice at the top surface is the sum of the conductive and ice heating heat flux components, so we have the boundary condition for the heat equation

$$F^\star_{\mathrm{c,N+1/2}} = F_{\mathrm{inrt}} + F^{\mathrm{top}}_c \,. \tag{15}$$

The approach used for solving the heat equation in the ice is to first solve for the surface and basal heat balance at time step n, Section 2.2.1, which gives values for the fluxes $F^{\mathrm{top}}_{\mathrm{c}}$ and F^{bot}_c. The heat equation in the ice is then solved for time step $n + 1$ by means of equations (10) – (15).

2.2 Heat budgets

2.2.1 Heat budget for the ice covered ocean fraction

The heat budget for the ice covered fraction is given by considering the vertical heat fluxes arising in the ice due to atmospheric, oceanic and ice heat fluxes. There are two separate interfaces which undergo melting or freezing, the surface of the ice/snow system, and the bottom of the ice.

Heat budget for the ice/atmosphere interface The exchange of heat between the atmosphere and the ice or snow depends on the heat flux components listed in the previous section and in Appendix A. The heat flux balance at the top surface is given by balancing these fluxes, and if necessary achieve this balance by melting the surface material. The heat flux at the surface is given as

$$F_{\rm net}^{\rm top} = F_c^{\rm top} + F_{\rm brine}^{\rm in} + F_{\rm brine}^{\rm out} + F_{\rm inrt} - F_{\rm L,srf} - F_{\rm r,srf} - F_{\rm s,srf} - F_{\rm e,srf} \tag{16}$$

The brine heat storage fluxes $F_{\rm brine}^{\rm in}$, $F_{\rm brine}^{\rm out}$, the latent ($F_{\rm e,srf}$), sensible ($F_{\rm s,srf}$), the short wave ($F_{\rm r,srf}$) and the long wave heat flux ($F_{\rm L,srf}$) are all described in Appendix A. All the heat flux components, except the latent heat flux $F_{\rm e,srf}$ and the brine heat flux $F_{\rm brine}^{\rm out}$, has at most a first order dependence on the surface temperature $T_{\rm srf}$. By ignoring the temperature dependence of $F_{\rm e,srf}$ and ignoring the heat flux $F_{\rm brine}^{\rm out}$ entirely (for the moment), the net heat flux at the surface can be written as a linear function of the surface temperature. By using these expressions, the algorithm used to deduce the surface heat balance and the associated surface temperature is given as

1 First, seek the solution which results in no melting of the surface material: $F_{\rm net}^{\rm top}(T_{\rm srf})\Delta t = 0$.

2a If the temperature which caused this balance is above the melting point, reset the surface temperature to the melting point T_m, and seek the heat balance by melting the surface material: $F_{\rm net}^{\rm top}(T_m)\Delta t = -L_{\rm srf}\,\rho_{\rm srf}\,\Delta h_{\rm srf}$. The heat of fusion of ice $L_{\rm i}$ is modified by the latent heat stored in the ice, Equation (94).

2b If the temperature reached by step 1, here denoted by $T_{\rm srf}^{\star}$ is below the melting point, and the brine heat storage $Q_{\rm brine}$ is not empty, then supply enough heat from the brine storage to keep the surface at the melting point, $\left(F_{\rm net}^{\rm top}(T_{\rm srf})^{\star} - F_{\rm net}^{\rm top}(T_m)\right) = F_{\rm brine}^{\rm out}$. Adjust the heat storage accordingly; $\Delta Q_{\rm brine} = -F_{\rm brine}^{\rm out}\Delta t$. This introduces a small error since the latent heat flux also depends on the temperature. An iterative approach can be applied to reduce this error.

Heat budget for the ice/ocean interface The heat fluxes at the lower interface are somewhat simpler than at the top surface, since there is no contribution from the brine heat store, and both melting and freezing are allowed at the bottom of the ice. The heat balance given at the bottom of the ice is

$$F_w + F_{\rm rw} - F_{\rm c}^{\rm bot} = F_{\rm net}^{\rm bot} = -L_{\rm i}\,\rho_i \frac{dh_{\rm i}}{dt}\,. \tag{17}$$

The heat flux from the ocean (F_w), and the short wave heat flux going through the ice ($F_{\rm rw}$) are described in Appendix A. One should note that in this approach, there is no need to calculate a bottom surface temperature, since it is fixed to the freezing point of seawater in the calculations. The heat of fusion of ice $L_{\rm i}$ is modified by the latent heat stored in the ice, Equation (94).

2.2.2 Heat budget for the open water fraction

The atmospheric heat input over open water is given by the following heat balance

$$-F_{\rm L,w} - F_{\rm s,w} - F_{\rm e,w} - F_{\rm r,w} = F_{\rm net,w}\,, \tag{18}$$

where the net heat flux at the ocean surface is introduced, $F_{\rm net,w}$. Depending on the state of the ocean surface, different approaches are followed.

Cooling/Heating only If the ocean temperature is above the freezing point, the heat flux entering the open water fraction is used entirely to cool or heat the ocean

$$F_{\rm wo} = F_{\rm net,w} \times (1-c) = -(1-c)c_{\rm pw}h_w\rho_w\frac{\partial T_w}{\partial t}\,, \tag{19}$$

where h_w is the thickness of the ocean layer below.

Lateral freezing of ice If the ocean surface is at the freezing point, further cooling of the ocean surface is compensated by latent heat loss due to freezing ice. The new ice introduced in this manner is set to have a thickness h_0, which means that the growth of new ice depends only on the lateral growth of the ice. For a unit area, which consists of both open water fraction $(1-c)$ and ice covered fraction (c), the total area of new ice created in the open water fraction becomes

$$F_{\rm wo} = F_{\rm net,w} \times (1-c) = -L_{0\rm i} h_0 \rho_i (1-c) \frac{\partial c_{\rm h0}}{\partial t} \tag{20}$$

In the multi-category ice model, newly frozen ice of thickness h_0 and concentration $c_{\rm h0}\Delta t$ accumulated over a time step Δt will be added to an already existing ice class. Which class depends on the discretization of the ice thickness and the choice of h_0, but it is usually the class with lowest ice thickness range, see Section 4.

3 Ice thickness distribution

The ice thickness distribution describes how the ice in a model grid cell is comprised of ice of different thicknesses. This description is important since ice of different thickness will give a different insulation of the underlying ocean. The model describes the ice thickness distribution as discrete ice thicknesses, each having an associated areal coverage. This is achieved by using δ-functions, and the theory of redistribution follows that of Thorndike et al. (1975), specially formulated for this choice of the thickness distribution model.

This section deals with the model description of the ice thickness distribution $g(h)$ and the so-called redistribution function $\psi(h)$.

3.1 Main equations

The ice thickness distribution $g(h)$ can be thought of as a probability function where $g(h)\mathrm{d}h$ gives the probability of finding ice in the thickness range $(h, h+\mathrm{d}h)$ over a given area. The zero and first order moments of the ice thickness distribution $g(h)$ are

$$\int_0^\infty g(h)\,\mathrm{d}h = 1 \qquad\qquad \int_0^\infty h\,g(h)\,\mathrm{d}h = \overline{h}\,, \tag{21}$$

where $\overline{h}$ is the mean thickness of ice in the area.

The evolution of the ice thickness distribution is given by the following equation from Thorndike et al. (1975)

$$\frac{\partial g}{\partial t} = -\nabla\cdot(\boldsymbol{v}g) - \frac{\partial}{\partial h}(f\,g) + \psi\,. \tag{22}$$

In this equation, $\boldsymbol{v}$ is the ice velocity and $f = \partial h/\partial t|_{h_i}$ is the growth rate of ice with thickness h_i. The distribution ψ is a function denoting ice redistribution due to ridging and rafting of ice.

Two constraints apply for the redistribution function ψ. First, by integrating Equation (22) we have

$$\int_0^\infty \psi \mathrm{d}h = \Psi(\infty) = \nabla\cdot\boldsymbol{v}\,, \tag{23}$$

where $\Psi(h) = \int_0^h \psi \mathrm{d}h$. Secondly, since the redistribution does not remove or introduce ice it should conserve volume,

$$\int_0^\infty h\psi \mathrm{d}h = 0\,. \tag{24}$$

The functional form of the redistribution function ψ depends on the motion of the ice, and is different for divergence and convergence. The form for these two situations will be given in Section 3.3.1 and 3.3.2.

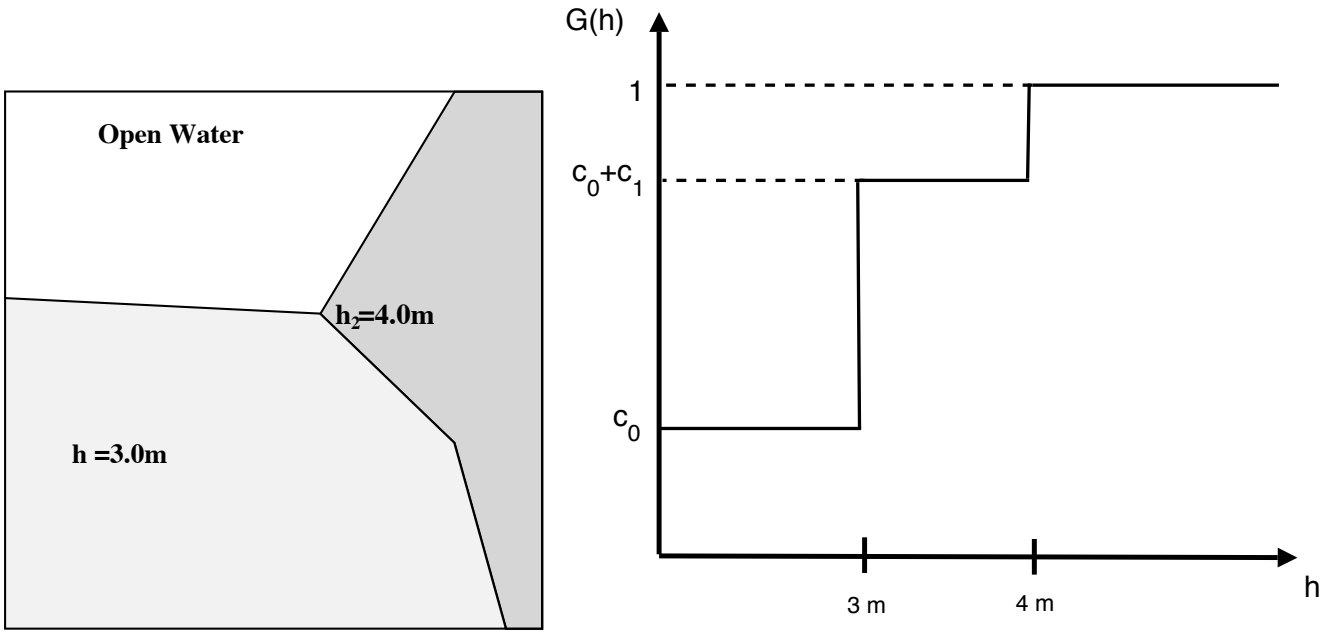

Figure 2: Illustration of the form of the ice thickness distribution used in the model. The ice cover is comprised of a set of ice floes with discrete ice thicknesses $h_i, i = 1, N$. Each collection of ice floes with ice thickness h_i has a fractional surface coverage of c_i. The illustration shows a model grid cell with three discrete ice thicknesses, and their possible spatial coverage. Shown here is one area with ice thickness of three meters, one four meters and one class for open water. The spatial organization of the ice floes in a grid cell is unspecified in the model, so the arrangement of the floes in the figure is only for illustration purposes. Right panel shows the cumulative ice thickness distribution resulting from the ice thickness distribution in the left panel.

3.2 Model description of $g(h)$

The approach used for modeling $g(h)$ in a grid cell is to describe it as a sum of fractional ice covers c_i, each having ice thickness h_i. The actual spatial distribution of the ice thickness within an area (such as a model grid cell) is unspecified by the model, but a conceptual illustration is shown in Figure 2.

The description of the ice thickness distribution can be achieved by using delta-functions. The distribution $g(h)$ and the cumulative distribution $G(h) = \int_0^h g(h)\mathrm{d}h$ become

$$g(h) = c_0\delta(h) + \sum_{i=1}^{N} c_i\delta(h - h_i) + \sum_{i=1}^{N} c_i^{\psi}\delta(\frac{h}{k} - h_i)\,, \text{ and} \tag{25}$$

$$G(h) = c_0\mathcal{H}(h) + \sum_{i=1}^{N} c_i\mathcal{H}(h - h_i) + \sum_{i=1}^{N} c_i^{\psi}\mathcal{H}\left(\frac{h}{k} - h_i\right)\,. \tag{26}$$

In Equation (26) $\mathcal{H}(h)$ is the Heaviside step-function, also note that we include fractions c_i^{ψ} which will be created by the ridging process, this will be useful later on.

Integrating Equation (22) from 0 to a thickness h gives an equation for the evolution of the cumulative thickness distribution

$$\frac{\partial G(h)}{\partial t} = -\nabla\cdot(\boldsymbol{v}G) + \sum_{i=1}^{N} c_i\delta(h - h_i)f(h) + \sum_{i=1}^{N} c_i^{\psi}\delta(\frac{h}{k} - h_i)f(h) + \Psi\,. \tag{27}$$

Taking the time derivative of Equation (26) gives yet another equation for the time evolution of

$G(h)$, so by combining that with (27) the following is obtained,

$$-\nabla \cdot (\boldsymbol{v}G) + \Psi = \frac{\partial c_0}{\partial t}\mathcal{H}(h) + \sum_{i=1}^{N} \frac{\partial c_i}{\partial t}\mathcal{H}(h - h_i) + \sum_{i=1}^{N} \frac{\partial c_i^{\psi}}{\partial t}\mathcal{H}\left(\frac{h}{k} - h_i\right) \tag{28}$$

which provides an evolution equation for the different ice fractions c_i in the distribution $g(h)$. The ridging processes will also create new fractions involved in $G(h)$, namely c_i^{ψ}. Note that all references to thermodynamic growth, $f(h)$, have been removed by combining the two equations for the ice thickness distribution. This allows for a relatively clean separation of the model into a thermodynamic part (Section 2) and a kinematic part.

3.3 The redistribution function ψ

The functional form of ψ for divergence and ridging will now be derived, again building on the theory of Thorndike et al. (1975).

3.3.1 Ice divergence

In this case, the ice transported out of a grid cell is replaced by open water. No other redistribution of ice thickness takes place. Therefore

$$\Psi = \mathcal{H}(h)\ \nabla \cdot \boldsymbol{v}\,, \tag{29}$$

which adheres to restriction (23). This gives, when inserted into Equation (28)

$$\frac{\partial c_i}{\partial t} = -\nabla \cdot (\boldsymbol{v}c_i) \tag{30}$$

$$\frac{\partial c_i^{\psi}}{\partial t} = 0 \tag{31}$$

$$\frac{\partial c_0}{\partial t} = -\nabla \cdot (\boldsymbol{v}c_0) + \nabla \cdot \boldsymbol{v} = (1 - c_0)\nabla \cdot \boldsymbol{v} + \boldsymbol{v} \cdot \nabla c_0 \tag{32}$$

3.3.2 Ice convergence

When the ice concentration is close to unity, continued ice convergence must be compensated for by rearranging the ice in a manner simulating sea ice ridging. The functional describing this redistribution has the form

$$\psi = w_r(h)\,\nabla \cdot \boldsymbol{v}\,. \tag{33}$$

Here the function w_r is called the ridging mode. Thorndike et al. (1975) splits the function w_r into two different parts, a source and a sink term. The sink term $a(h)$ describes the fraction of ice which is ridged, while the distribution $n(h)$ describes the new fraction of ice which is the result of this ridging. The form will be discussed briefly here for our application.

The ice participating in ridging is given as

$$a(h) = b(h)\,g(h), \tag{34}$$

where $b(h)$ is a weighting function, having the effect of emphasizing the thin end of the ice thickness distribution $g(h)$. It is given as a piecewise linear function of h, from (Thorndike et al., 1975)

$$b(h) = \frac{2}{G^{\star}}\left[1 - \frac{G(h)}{G^{\star}}\right] \qquad 0 \le G(h) \le G^{\star}\,, \tag{35}$$

$$b(h) = 0 \qquad G^{\star} < G(h)\,. \tag{36}$$

$G^\star$ is the cumulative fraction below which all ridging is set to occur, a threshold value set by Thorndike et al. (1975). It should be noted that because of this, no ridging will occur if the open water in a grid cell exceeds $G^\star$.

The choice of the linear function $b(h)$ normalize $a(h)$ so that its integral over all h is unity when $g(h)$ is a continuous or piecewise continuous function. The distribution $g(h)$ is here described with delta–functions, so an adjustment of $g(h)$ used in ridging is needed. This is done by only ridging a fraction of the ice in the range $(h_i - \epsilon, h_i + \epsilon)$ when $G(h_i - \epsilon) < G^\star < G(h_i + \epsilon)$. To accomplish this, the ice thickness distribution available for ridging, denoted $g^r(h)$, is introduced

$$g^r(h) = c_0\delta(h) + \sum_{i=1}^{N} c_i^r \delta(h - h_i) \tag{37}$$

where

$$c_0^r = \min(G^\star, c_0) \tag{38}$$

$$c_k^r = \min(G^\star, \sum_{i=0}^{k} c_i) - \min(G^\star, \sum_{i=0}^{k-1} c_i) \qquad \text{where } k \in 1, 2, \ldots, N \tag{39}$$

The cumulative distribution corresponding to Equation (34) becomes,

$$A(h) = \int_0^h b(h')g^r(h')\mathrm{d}h' = \sum_{i=0}^{N} b(h_i)c_i^r \mathcal{H}\left(h - h_i\right) , \tag{40}$$

The redistribution $n(h)$ of the ice is determined by the redistribution process $\gamma(h_1, h_2)$. The redistribution process used here is identical in form to the one used in Thorndike et al. (1975),

$$\gamma(h, h_r) = \frac{1}{k}\delta(h_r - k\,h) \text{ where } k > 0\,, \tag{41}$$

where the ridging produces ice of thickness h_r which is k times the thickness of the original ice (h). The only difference is that k is allowed to be a random Gaussian distributed variable of mean 10 and standard deviation 2. The mean value of the ridging coefficient is somewhat higher than values used by Thorndike et al. (1975). The newly ridged ice is calculated by integrating $\gamma(h, h_r)$ multiplied with the ice available for ridging, $a(h)$

$$n(h_r) = \int_0^\infty \gamma(h, h_r)a(h)\mathrm{d}h = \frac{1}{k^2}a\left(\frac{h_r}{k}\right) . \tag{42}$$

The cumulative distribution corresponding to this becomes

$$N(h) = \int_0^h n(h')\mathrm{d}h' = \frac{1}{k}A\left(\frac{h}{k}\right) = \frac{1}{k}\sum_{i=0}^{N} b\left(h_i\right) c_i^r \mathcal{H}\left(\frac{h}{k} - h_i\right) \tag{43}$$

The ice thickness redistribution w_r should be set up to satisfy (23). For the cumulative ridging mode W_r this is equal to $W_r(\infty) = 1$. This can be achieved by giving $W_r(h)$ as

$$W_r(h) = \frac{\int_0^h -a(h) + n(h)\mathrm{d}h}{\int_0^\infty -a(h) + n(h)\mathrm{d}h} = \frac{-A(h) + N(h)}{-A(\infty) + N(\infty)} \tag{44}$$

$$= \frac{1}{(-1 + 1/k)\sum_{i=1}^{N} b(h_i)c_i^r} \times \left[-\sum_{i=1}^{N} b(h_i)c_i^r \mathcal{H}\left(h - h_i\right) + \frac{1}{k}\sum_{i=1}^{N} b(h_i)c_i^r \mathcal{H}\left(\frac{h}{k} - h_i\right)\right] \tag{45}$$

By letting $\Psi(h) = W_r(h)\nabla \cdot \boldsymbol{v}$ and putting this into Equation (28), the equations for the fractions c_i and c_i^ψ become

$$\frac{\partial c_i}{\partial t} = -\nabla \cdot (\boldsymbol{v} c_i) - \frac{\nabla \cdot \boldsymbol{v}}{(-1 + 1/k)\sum_{i=1}^{N} b(h_i)c_i^r} b(h_i)c_i^r \,, \tag{46}$$

$$\frac{\partial c_i^\psi}{\partial t} = \frac{\nabla \cdot \boldsymbol{v}}{(1-k)\sum_{i=1}^{N} b(h_i)c_i^r} b(h_i)c_i^r \,, \text{ and} \tag{47}$$

$$\frac{\partial c_0}{\partial t} = \sum_{i=1}^{N} \left(\frac{\partial c_i^\psi}{\partial t} - \frac{\partial c_i}{\partial t} \right) . \tag{48}$$

This provides convenient equations for the evolution of existing fractions c_i and the creation of new fractions c_i^ψ of thickness kh_i. However, this procedure can create an indefinite number of δ-functions describing $g(h)$. To avoid this, restrictions are imposed on $g(h)$, and "ice classes" are introduced in the next section.

4 Managing the ice thickness distribution

This section deals with the practical aspects of describing the ice cover with a set of delta-functions, as described in Section 3. Ice categories are introduced as a book-keeping measure, serving to limit the number of delta-functions describing the ice thickness distribution $g(h)$. In addition, the ice categories are implemented so that each ice category can have a different setup of the ice thermodynamics (ref. thin and thick ice setups in Section 2).

4.1 Introducing Ice categories

For practical purposes, constraints are imposed on the form of $g(h)$. As seen in Section 3, the redistribution of ice with thickness h will create new ice of thickness kh. This in effect creates new additions of δ-functions in the ice thickness distribution $g(h)$. Over time this means that the number N of delta functions will grow indefinitely, which is impractical.

In order to deal with this, ice categories are introduced. A number of thickness limits are specified in order to divide the ice into different categories, the limits are given as H_i, where $i \in 1, \ldots, N$. Ice in category number i is then given as the ice with thickness h_i such that

$$H_i < h_i < H_{i+1} \qquad i \in [1, \ldots, N-1] \tag{49}$$

$$H_N < h_i \qquad i = N \,. \tag{50}$$

The restriction put on the ice distribution is now that at most one δ-function can exist within each ice thickness category limit. That means that the number of δ-functions describing ice of thickness $h > 0$ can be at most N. An example of such a ice thickness distribution is given in Figure 3.

The procedure taken if an ice thickness category $H_i < h < H_{i+1}$ becomes populated with two ice thickness delta-functions will be described. This can happen due to thermal growth or due to redistribution of ice. In this case two delta-functions will have to be combined into one.

4.2 Changing and combining ice

When ice is ridged, or ice grows thermodynamically, situations will arise where there are two ice thickness delta-functions occupying the same ice thickness range $[H_i, H_{i+1})$. In this case they must be added together to form one ice thickness delta function. This is particularly important for ridging processes, since ridging will create new ice thicknesses all the time.

In order to combine two delta functions into one, two things must be considered. First the ice thickness categories must be set to have the properties defined in the thickness range $[H_i, H_{i+1})$, this

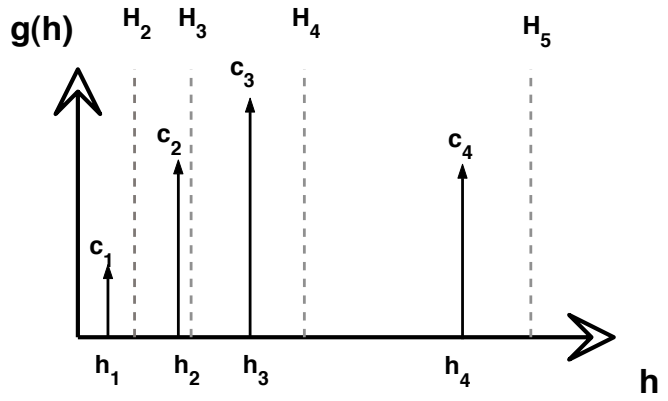

Figure 3: illustration of the form of the ice thickness distribution used in the model. Each of the ice thicknesses delta-functions has a concentration c_i, and the delta functions for ice thickness h_i are denoted by arrows. An ice thickness category is defined as the region within each thickness limit $[H_i, H_{i+1})$, and only one delta-function can exist in that thickness range.

in effect means that the number of layers in the ice must correspond to the number of thermodynamic layers defined for the category, as each ice category can have a different number of layers in the vertical. Secondly the two delta-function descriptions must be added in a consistent manner.

4.2.1 Changing ice categories

In order to change the ice into having the properties of a new ice category, a suitable change of temperatures in the ice must be done. These changes should conserve the thermal energy of the ice, and should also keep a similar vertical temperature profile in the ice.

Let the old temperature profile be piecewise linear with height z. The temperature profile of the ice is defined through its layer bulk temperature $T_{\mathrm{i,m}}$, given as the temperature of ice layer midpoints. In each layer m a linear temperature profile is assumed

$$T_i^{\mathrm{old}}(z) = a_m + b_m\left(z - (m-1)\Delta z_{\mathrm{old}}\right) \qquad z \in [(m-1)\Delta z_{\mathrm{old}}, m\Delta z_{\mathrm{old}}) \tag{51}$$

$$a_m = \frac{T_{\mathrm{i,m-1}} + T_{\mathrm{i,m}}}{2} \qquad m \in [2, N^{\mathrm{old}}] \tag{52}$$

$$a_0 = T_0 - (T_1 - T_0) = 2T_0 - T_1 \tag{53}$$

$$b_m = \frac{T_{\mathrm{i,m}} - a_m}{\Delta z_{\mathrm{old}}/2} \qquad m \in [1, N^{\mathrm{old}}] \tag{54}$$

This function is piecewise linear in the ice, with a temperature average in each layer of $T_{\mathrm{i,m}}$. Changing the number of layers from N^{old} to N^{new} gives new layer thicknesses; going from $\Delta z_{\mathrm{old}} = h_i/N^{\mathrm{old}}$ to $\Delta z_{\mathrm{new}} = h_i/N^{\mathrm{new}}$. The new layer temperatures are calculated by integrating the piecewise linear function $T_i^{\mathrm{old}}(z)$ over each of the new layers:

$$T_{i,m}^{\mathrm{new}} = \frac{1}{\Delta z_{\mathrm{new}}} \int_{(m-1)\Delta z_{\mathrm{new}}}^{m\Delta z_{\mathrm{new}}} T_i^{\mathrm{old}}(z)\mathrm{d}z \quad m \in [0, N^{\mathrm{new}}]\,, \tag{55}$$

giving the new temperature profile for the ice. All the surface properties are kept at their old values when changing an ice category. This can create a slight flux imbalance at the surface, since the conductive heat flux will change because of this.

4.2.2 Adding ice categories

Only one ice thickness delta-function is allowed to exist in a certain thickness range. Therefore, when two or more ice delta-functions are present in a thickness range they will have to be added

together to form a single category. Consider two different ice thickness delta-functions within a ice thickness category

$$g(h) = c_1\delta(h - h_1) + c_2\delta(h - h_2)\,. \tag{56}$$

The functional is combined to form one ice thickness delta function, using the following equations,

$$c^{\text{new}} = c_1 + c_2 \tag{57}$$
$$h^{\text{new}} = \left(h_1c_1 + h_2c_2\right)/c^{\text{new}} \tag{58}$$
$$h_s^{\text{new}} = \left(h_{s_1}c_1 + h_{s_2}c_2\right)/c^{\text{new}} \tag{59}$$
$$\rho_s^{\text{new}} = \left(\rho_{s_1}h_{s_1}c_1 + \rho_{s_2}h_{s_2}c_2\right)/\left(c^{\text{new}}h_s^{\text{new}}\right) \tag{60}$$
$$T_{i,m}^{\text{new}} = \left(h_1T_{i,m}^1c_1 + h_2T_{i,m}^2c_2\right)/\left(h_1c_1 + h_2c_2\right) \tag{61}$$
$$Q_{\text{brine}}^{\text{new}} = \left(c_1Q_{\text{brine},1} + c_2Q_{\text{brine},2}\right)/c^{\text{new}}\,. \tag{62}$$

Here Q_{brine} is the heat stored in the brine storage, and ρ_s is the density of snow. The new distribution is now given as

$$g(h)^{\text{new}} = c^{\text{new}}\delta(h - h^{\text{new}})\,. \tag{63}$$

4.3 Redistribution and thermodynamics

As seen in Section 3, there is a clean separation between the thermodynamic and kinematic components of the sea ice model. This separation means that the evolution of the ice cover is managed by two separate routines. Consider the functional description of the ice thickness distribution:

$$g(h) = c_0\delta(h) + \sum_{i=1}^{N} c_i\delta(h - h_i) + \sum_{i=1}^{N} c_i^{\psi}\delta(\frac{h}{k} - h_i) \tag{64}$$

The thermodynamic part of the model will only modify the ice thickness h_i in the first sum in this equation. The redistribution part acts to create new fractions c_i^{ψ} due to ridging and reducing the existing fractions c_i accordingly. In addition to this comes the effects of ice advection. This separation between thermodynamics and kinematics has proved to be very convenient when implementing the actual model code.

5 Baseline model results

This section presents results from an application of the sea ice model. The model is coupled to an ocean model and ice dynamics model. Comparisons are done with some of the sparsely available data for the Arctic. Sensitivity experiments are also performed to examine the impact of varying the number of ice thickness categories.

5.1 Implementation with HYCOM

The sea-ice model has been coupled to the HYbrid Coordinate Ocean Model (HYCOM; Bleck, 2002). HYCOM can use a mixture of sigma, z and isopycnic coordinates to describe the ocean in the vertical, and has several options for vertical mixing schemes. HYCOM, as set up here has z-layers with five meter resolution near the surface. Deeper in the water column the z-layers smoothly revert to isopycnal layers in the ocean interior. The model uses 22 layers in the vertical with densities ranging from 1021 to 1028.11 $\mathrm{kg\,m^{-3}}$ referenced to potential density at the surface, where the lightest layers become z-layers in the hybrid coordinate formulation. The thermobaricity parameterization of Sun et al. (1999) is also used. For vertical mixing the K-Profile Parameterization scheme of Large et al. (1994) is used.

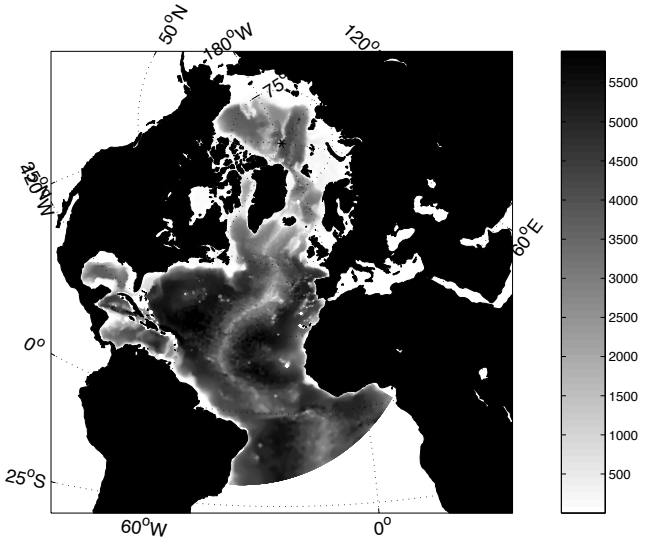

Figure 4: Illustration of the model grid used in the experiments, the grid covers the North Atlantic and Arctic ocean with grid sizes between 50-80 km for these regions.

Ice thickness class	1	2	3	4	5
Ice thickness limits	0-0.5 m	0.5-1.0 m	1.0-2.0 m	2.0-5.0 m	+5.0 m
Vertical layers	1	1	3	4	5

Table 1: The table shows the number of ice categories used in the model, the ice thickness limits for each class and the number of vertical layers used when solving the thermodynamics.

The model grid is set up using the conformal mapping tools of Bentsen et al. (1999), with a grid size ranging from 50 to 80 km in the North Atlantic and Arctic regions, see Figure 4. To calculate heat fluxes the simulation uses reanalyzed data (ERA40) from the European Center for Medium-Range Weather Forecasts (ECMWF). Data used from the ERA40 data set are temperature at 2 meters, dew-point temperature at 2 meters, winds at 10 meters, clouds and precipitation. Rivers are included and added to the model fields as a negative salinity flux.

The sea ice model uses the thermodynamic model given in Section 2, and the ice thickness distribution formulation given in Sections 3 and 4. The dynamic part of the ice model uses the EVP formulation of Hunke and Dukowicz (1997). In the baseline experiment, a total of 5 ice thickness categories are used to account for the different ice thicknesses encountered in the Arctic ocean, see Table 3. Later on, in Section 6, sensitivity experiments will be done where the number of ice thickness categories are changed. The thickness classes are closer for the thin end of the thickness distribution, whereas ice thickness greater than 5 meters makes up the last class. The thickness limit used to delimit "thick" and "thin" ice in the thermodynamic model (h_L) is set to 1.0 meters. In ice classes 3-5 the heat equation is solved explicitly, whereas for class 1-2 it is solved using the parameterizations given for "thin ice". The coupling between the ice model and HYCOM involves the transfer of ocean heat and salinity fluxes calculated from the ice model to HYCOM. In addition there is a two-way exchange of drag forces acting between the ice and the ocean.

The coupling between the ice model and HYCOM involves the transfer of ocean heat and salinity fluxes calculated from the ice model to HYCOM. In addition there is a two-way exchange of drag forces acting between the ice and the ocean. The drag from the ocean on the ice, and from the atmosphere on ice is given by quadratic bulk formulas as

$$\tau_{i,o} = \rho_w C_{\mathrm{D,o}} \left(\boldsymbol{v}_o - \boldsymbol{v}_i\right) \left|\boldsymbol{v}_o - \boldsymbol{v}_i\right| , \tag{65}$$

$$\tau_{i,a} = \rho_a C_{\mathrm{D,a}} \boldsymbol{v}_a \left|\boldsymbol{v}_a\right| , \tag{66}$$

where the drag coefficients are set to $C_{\mathrm{D,o}} = 5.5 \times 10^{-3}$ and $C_{\mathrm{D,a}} = 2.2 \times 10^{-3}$, and a zero turning

angle is assumed. The EVP model is set up with the ice strength parameterization of Hibler III (1980), given as

$$P = P^{\star} c\overline{h} e^{-C^{\star}(1-c)}, \tag{67}$$

where $P^{\star} = 27500\mathrm{Nm}^{-2}$, and $C^{\star} = 20$. The sea ice model thermodynamics are tightly coupled to the ocean model, and the ice model calculates the heat fluxes to the ocean model for every ocean model time step. The EVP model, ridging, and advection of sea-ice parameters are done every two hours. Sea ice shear does not contribute to ridging in the simulations. Also, it should be mentioned that the model at present has no separation between ridge or unridged ice.

The ocean model was initialized from the Generalized Digital Environment Model (GDEM, Teague et al., 1990) climatology, and run with ERA40 forcing from 1958 until 2002 after a 10 year spin-up using a ERA40-based climatology. During the integration the model was run using surface salinity and temperature relaxation with an e-folding time scale of 150 days. This relaxation was only applied in ice-free areas. Along the model boundaries (Bering Strait, South Atlantic ocean) the model was relaxed towards the GDEM climatology. In addition, the model was set up with a 0.8 Sv barotropic transport into the Arctic from the Bering Strait (Woodgate et al., 2005).

5.2 Model results and discussion

The mean summer (July-September) and mean winter (January-March) ice thickness fields were calculated for the time period 1958–2002 and are shown in Figures 5(b) and 5(a). The ice thickness

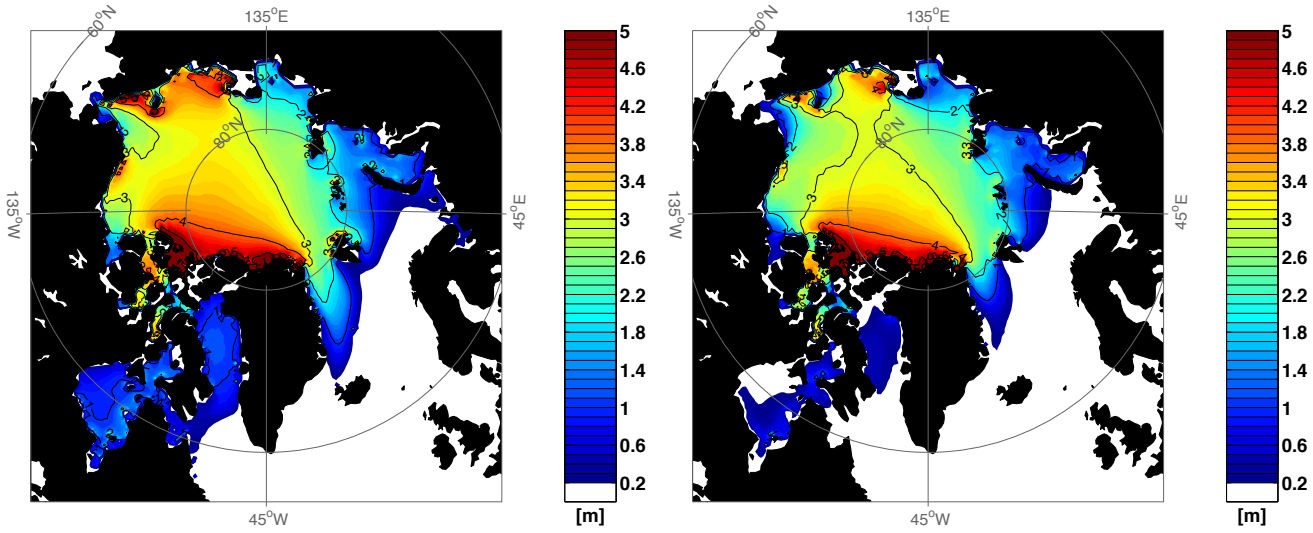

(a) January-March Ice Thickness

(b) July-September Ice Thickness

Figure 5: Mean ice thickness for for the period 1958–2002.

fields are reasonable, increasing in thickness from the Siberian Coast towards the Canadian Arctic Archipelago and the northern coast of Greenland. Thick ice is present in the Beaufort Sea, and the East Siberian Sea also has relatively thick ice. Sea ice transport through the Fram Strait is illustrated by the tongue of thicker ice being advected from the Arctic Basin into the Greenland Sea.

Ice concentration is not shown, but at times the ice extent can be excessive in the peripheral seas of the Arctic, such as the Barents Sea and the Greenland Sea. The overestimated ice extent in these seas is partly connected to too low inflow of Atlantic Water into the Nordic Seas. The inflow of warm Atlantic water into the Nordic Seas is about 6 Sv which is lower than estimates from models (Nilsen et al., 2003) and observations (Østerhus et al., 2005) of 8 Sv. Another possible mechanism could be too high transport of sea ice from the Arctic into the Greenland Sea, but ice transport estimates shown later on show that this is probably not the case.

The ice thickness distribution is described using a set of ice thickness classes in the model. Figure 6 shows a monthly average of the ice fraction making up ice class 4, and the corresponding ice thickness of class 4. Note how the ice thickness is allowed to vary between the limits set for the class (2 to 5 meters). For ice class 4, the greatest fractional coverage can often be found north of

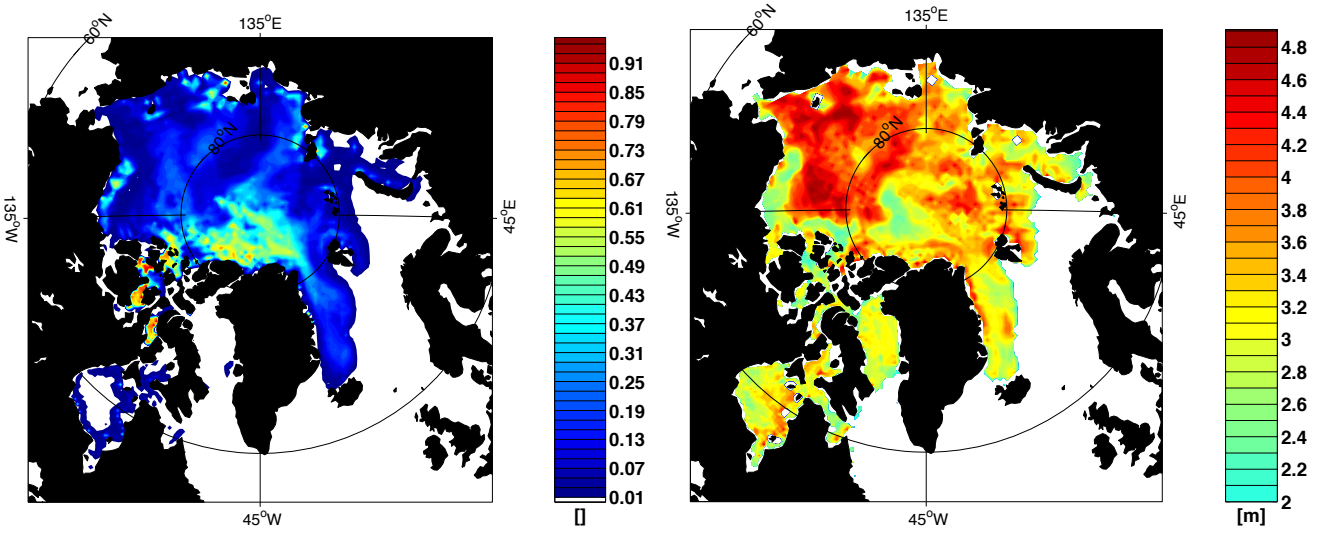

(a) Ice fraction of ice class 4 (c_4)

(b) Ice thickness of ice class 4 (h_4)

Figure 6: Illustration of the ice making up ice class 4 (ref Table 3). The illustration is from the monthly average of February 1983.

Greenland, as in Figure 6(a). This happens because ice ridging occurs there, and the ice thickness range for class 4 covers 2-5 meters. The highest thickness values in this range are usually due to ice ridging.

Class 4 ice is also present close to other land boundaries in the Arctic, as well as in the transpolar drift stream region. It can also be found in the Beaufort Sea, although to a smaller degree than might be expected. The ice thickness and fractional coverage of class 4 ice is quite low in some regions close to the northern coast of Greenland, the reason for this is a high coverage of thicker class 5 ice in that region.

5.2.1 Comparison with ULS data

A more rigorous look at the modeled ice thickness fields can be done by comparing with data gathered from Upward Looking Sonars (ULS) carried on board British and American submarines. The sea ice draft data gathered from submarines is provided by the National Snow and Ice Data Center (NSIDC) for several cruises from the 1970s up until the 1990s.

The ULS data consists of a collection of files where each file provides a "track". This is a collection of ice draft measurements over a given track length, typically 50 km, although this length can vary. Track lengths from the "SCICEX" cruises, for instance, are typically of 12 km length. Averaged ULS ice draft is calculated for a track and is compared to the model mean ice draft estimate, where the model ice draft h_d is calculated as

$$h_d = \frac{\sum_{j=1}^{N} c_j \left(\rho_i h_j + \rho_{s,j} h_{s,j}\right)}{\rho_w}. \tag{68}$$

The ice draft from the model is based on weekly averages of ice and snow thickness, and snow density. The model fields are interpolated to the positions of the observed tracks, to create "simulated" cruise tracks.

Three example cruises illustrating the difference between model and ULS draft measurements are shown in Figures 7(a), 7(d) and 7(g) for the submarine cruises denoted "1986a", "1991" and

"1993" respectively. They illustrate that the model gives a favorable description of the sea ice draft. Cruises "1986a" and "1993" show the best correspondence between model and data. The short scale variability is not captured by the model, nor do we expect it to be due to low spatial and temporal resolution, but the large scale variations in sea ice draft correspond well with the ULS data. On the other hand, data from the cruise "1991" shows a situation where the model does not capture the large scale variability that well. In this case there is a positive bias in the ice draft field when considering the thickness field along the entire track.

Cruise	UK76	1986a	1986b	1987	UK87	1988a	1988b
RMS error	0.54	0.23	0.98	0.74	2.06	0.23	0.91
Bias	0.66	-0.03	-0.83	-0.63	0.21	0.09	-0.85

Cruise	1989b	1990	1991	UK91	1992a	1992b	L2-92
RMS Error	0.46	0.18	0.49	0.80	0.47	0.31	0.65
Bias	0.13	0.14	0.42	-0.36	-0.29	0.34	0.58

Cruise	grayling92	1993	scicex93	1994	scicex96	scicex97	scicex98
RMS Error	0.64	0.16	0.58	0.20	0.40	0.83	0.45
Bias	-0.52	0.21	0.60	0.24	0.30	0.70	0.17

Table 2: Difference between simulated tracks and the tracks provided by the NSIDC. Table shows the Root-Mean-Square(RMS) difference and the average difference between tracks.

Table 2 shows the RMS errors and the bias of the model when compared with all the available ULS data. From the table the ice thickness bias is positive for some cruises and negative for others, there is no strong overall bias in either direction. Some cruises stand out in the table, the cruise "1986b" has a draft underestimate which is consistent for the entire cruise track, giving a negative bias and a RMS error of nearly one meter. The cruise "scicex97" also has relatively high errors, due a positive bias for that cruise.

The cruise "UK87" also stands out in Table 2, having a small bias, but a very large RMS error. It turns out that this RMS error stems from a very high track-to-track variability in the ice field for this cruise, this variability is not captured by the model, Figure 8(a). The "UK87" cruise was carried out in the Fram Strait as was the "UK91" cruise, Figure 8(b). The UK91 cruise shows much lower short-scale variability than the "UK87" Cruise, and the model does well in simulating the UK91 cruise. It should be noted that the track lengths of the ULS data are the same in both the "UK87" and "UK91" cruises, so the differences in track-to-track variability point to changes in the ice field which are not captured by the model. One reason for this could be low spatial resolution in the model and sub-grid scale processes.

To sum up all the different comparisons of ice draft a scatter plot for the ULS draft vs. model draft is shown in Figure 9 for all available cruises. The color indicator denotes the month of the measurement. Again, the model is able to reproduce the ULS ice thickness data for most of the cruises seen here. It should be noted, however, that the model has a tendency to produce too thick ice in the ULS 1-2m thickness range. This appears mainly due to summer cruises, most noticeably the "scicex97" cruise.

The ice draft distribution is readily obtained from the ULS data. To compare this with the model data, it is convenient to change this to a cumulative ice draft distribution. The average cumulative draft distributions for the cruises "1986a", "1991" and "1993" are shown in Figures 7(c), 7(f) and 7(i) respectively.

Although the model CDF is smoothed over several tracks (several grid cells), the staircase-like behavior which is to be expected for a single model CDF is still visible. This is most pronounced for the "1991" and "1993" cruises. Nonetheless, the model CDF corresponds quite well when compared to the ULS-derived CDF. From the comparison it can be seen that the model in some cases puts too

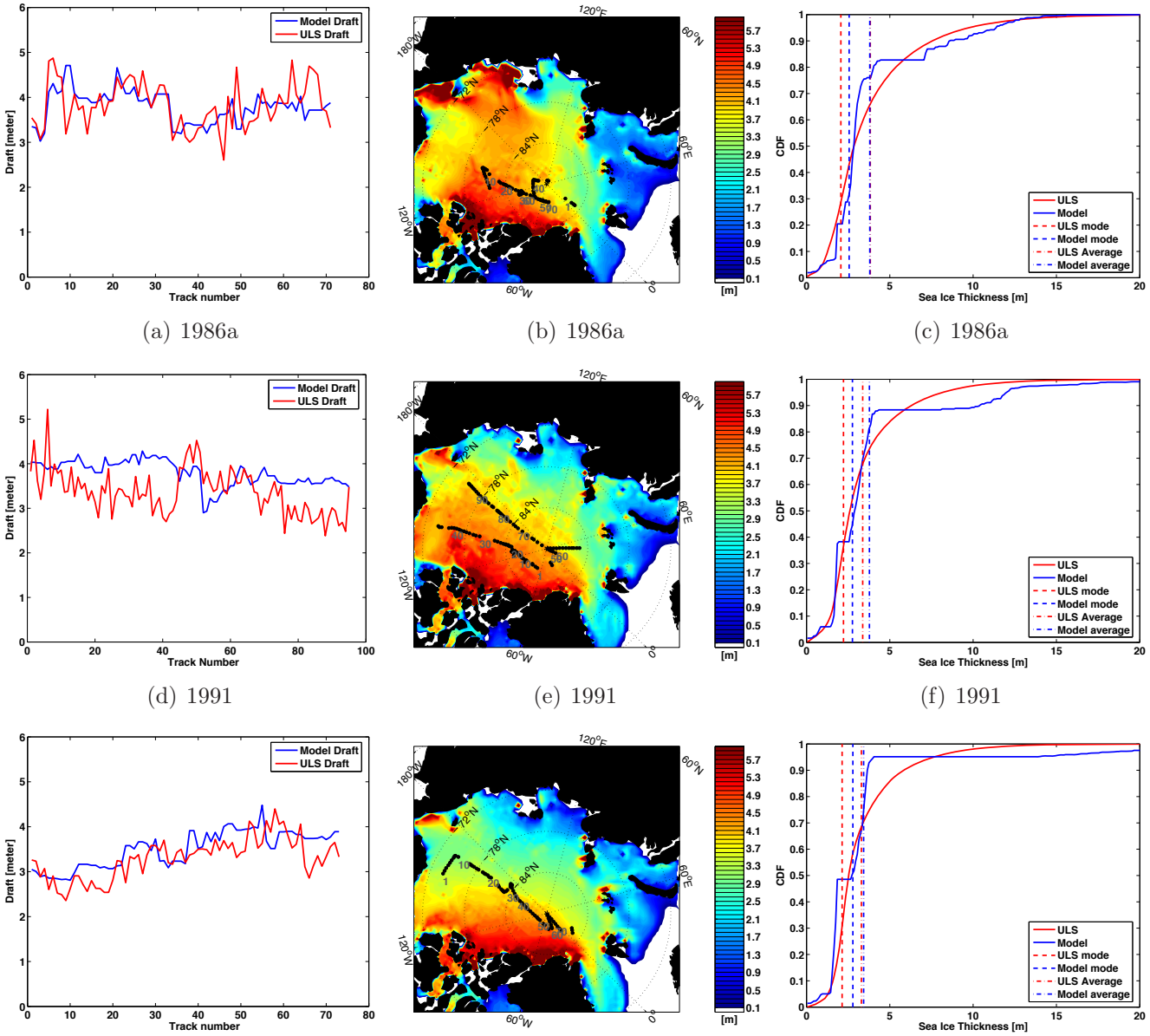

(a) 1986a (b) 1986a (c) 1986a

(d) 1991 (e) 1991 (f) 1991

(g) 1993 (h) 1993 (i) 1993

Figure 7: Left panel shows the ice draft from model (red) and data (blue) for three different tracks. Right panel shows spatial location where color indicates difference (model -data). From top to bottom the cruises are: "1986a", "1991", and "1993".

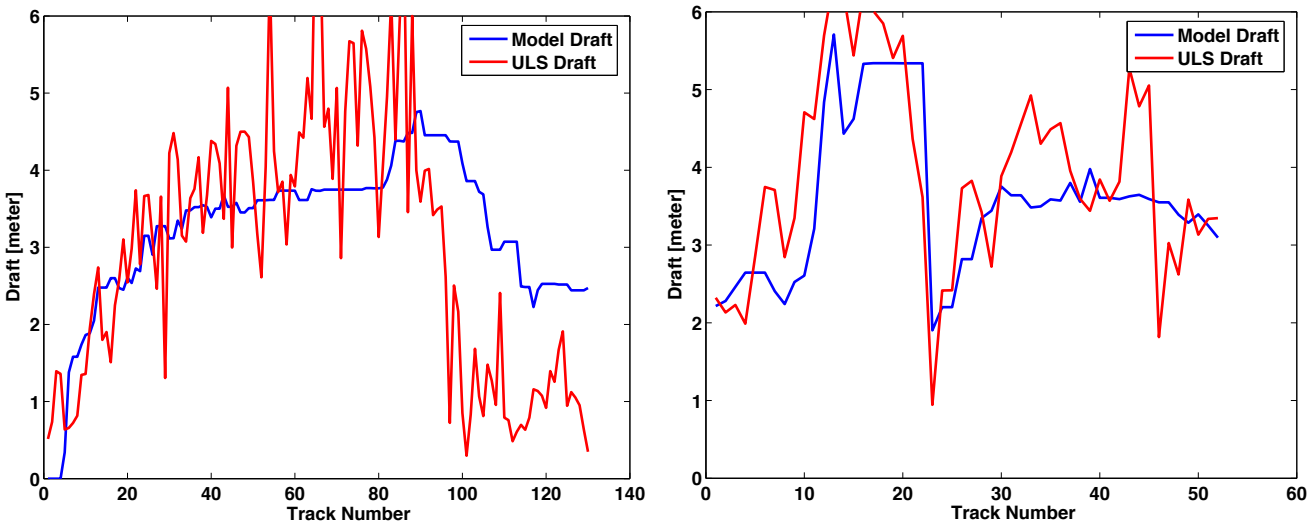

(a) UK87 (b) UK91

Figure 8: Ice draft from model (red) and data (blue) for two cruises carried out in the vicinity of the Fram Strait.

much ice in the thick end of the CDF, this is best seen for tracks "1991" and "1993". A reason for this could be the relatively high value used for the ridging parameter k, although runs with a lower value of k (6 as compared to 10) show very little difference.

5.2.2 Fram Strait transport

Another source of model validation is the ULS data in the Fram Strait from Vinje et al. (1998). The flux through this strait is responsible for the majority of the ice export out of the Arctic Basin, and is important for the ice mass balance of the Arctic Ocean and the deep and intermediate water production in the Greenland Sea. Figure 10 shows the net transport of sea ice through the Fram Strait and into the Greenland Sea. The figure illustrates both the volume and mass transports from the model, along with estimates from Vinje et al. (1998), shown by solid dots.

The modeled inflow from the Arctic varies significantly from year to year and on longer time scales. The ice volume transport through the Fram Strait varies between 1000 to 3000 $\mathrm{km}^3\,\mathrm{year}^{-1}$ for the annual average. Compared to data presented by Vinje et al. (1998), the volume exports are somewhat lower. However, the model values are reasonable, given the uncertainty in the measurements of Vinje et al. (1998).

A distinct feature in the ice transport time series is the maxima in 1995. The relatively high ice transport out of the Fram Strait in the 1990s also corresponds with a modeled record low ice mass in the Arctic in 1996 (not shown), similar to other model studies, see Rothrock et al. (2003). The modeled minima in sea ice volume occurs after the winter 1994-1995, when the sea ice volume transport was at its highest.

The 1995 peak in both ice and volume transports is also seen in the observation-based estimates of Vinje et al. (1998). However, even though the peak is present in the model, it is somewhat lower than the observation-based estimates. The bias estimates from the cruises, Table 2 indicate that the modeled ice mass in the Arctic is too thick for this time period. The underestimated ice transport through the Fram Strait is therefore likely to be related to too low drift rates across the Fram Strait section.

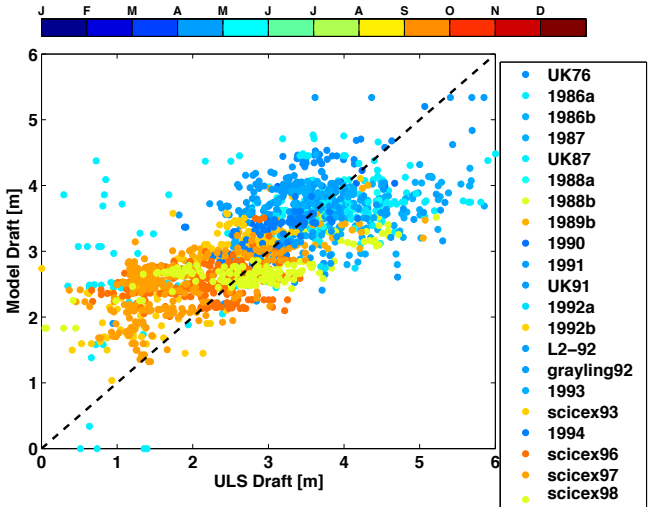

Figure 9: Scatter plot of ice draft from ULS measurements (horizontal axes) against model estimated draft (vertical axes). Color code denotes month of measurements.

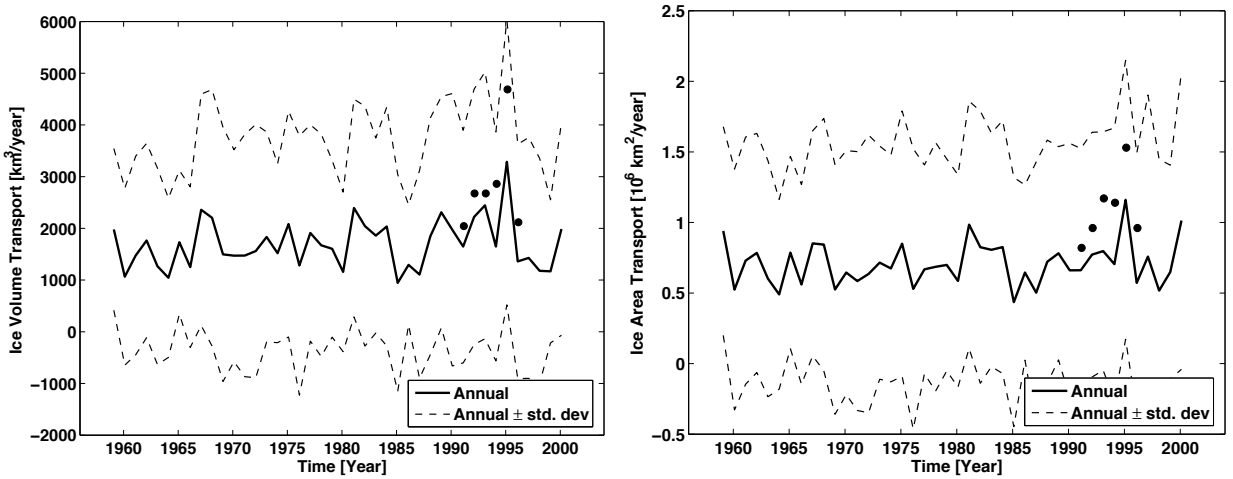

(a) Ice Volume Export

(b) Ice Area Export through Fram Strait

Figure 10: Panel 10(a) shows the transport of ice southward through the Fram Strait. The solid line shows the annual average (August to August) while the dashed line show annual average ± one standard deviation. Solid dots are corresponding estimates from Vinje et al. (1998). Panel 10(b) shows corresponding plot for ice area transport.

N	Upper ice category limits[m] (**number of categor y layers**)									
1	∞ (**1**)									
2	2.0(**1**)						∞ (**3**)			
5	0.5(**1**)		1.0 (**1**)		2.0(**3**)		5.0(**4**)		∞(**5**)	
10	0.25(**1**)	0.5(**1**)	0.75(**1**)	1.0(**1**)	1.5 (**3**)	2.0(**3**)	2.5(**4**)	5.0(**4**)	9.0(**5**)	∞(**5**)

Table 3: The table shows the upper limit of the different ice categories, and the number of vertical layers used to solve the heat equation in each category (in bold face and parentheses) for the sensitivity experiments. The "thin" ice description is used when the number of vertical layers is equal to one.

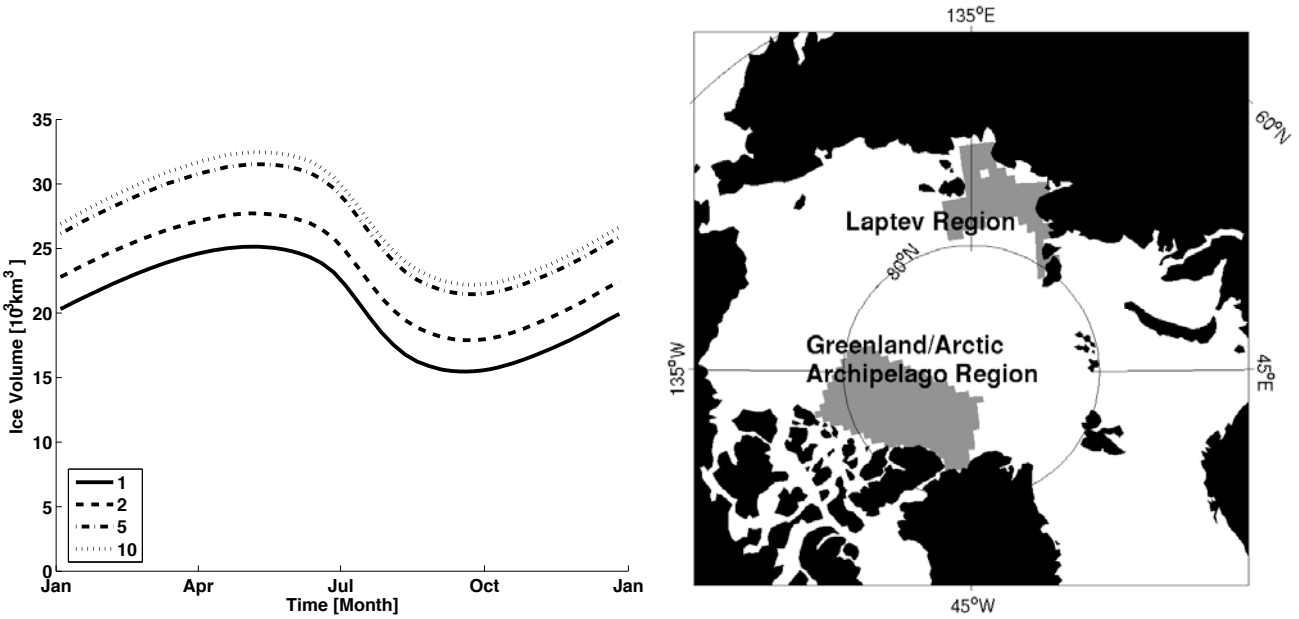

Figure 11: Left:Averaged yearly ice volume cycle for the different experiments. Legend indicates number of ice categories. Right: Region masks used in the sensitivity tests, two regions are defined, one North of Greenland and the Canadian Arctic Archipelago, One for the Laptev Sea, limited to the North by the 300m isobath.

6 Sensitivity experiments

This section presents results from the sensitivity experiments, and look at the differences in the total and local sea ice coverage of the model. In Section 6.1 average annual cycles are used to illustrate the differences between the experiments in two areas, one North of Greenland, and one focused on the Laptev Sea. In Section 6.2 a comparison with data from upward looking sonars is shown.

Four experiments were done, using different number of sea ice categories, but otherwise with the same setup as in the baseline experiment 3. The upper ice thickness limit of each category, and the number of vertical layers in the ice for each category is given in Table 3.

The average annual cycle of ice volume for the different experiments is shown in Figure 11. The figure illustrates how a better representation of the ice thickness distribution leads to an increased ice volume in the Arctic. This is primarily an effect of a higher ice thickness. The annual cycles are similar, although there is a slight phase and amplitude difference between the simulations with a large number of ice thickness categories, and those with few ice thickness categories.

The increasing ice thickness with higher ice thickness resolution is not surprising, and has previously been shown for multi-category models (Schramm et al., 1997; Bitz et al., 2001; Lipscomb, 2001). In the following we will illustrate how the ice mass changes on regional scales. The main

reason for the changes will be examined in Section 7.

6.1 Seasonal cycle of the ice cover

In order to look at the effect of resolving the ice thickness distribution, two separate regions are considered. The first region is centered on the Laptev Sea, bounded by the 300 m isobath. This region is a net source of Arctic sea ice, and a lot of the ice is transported from this region towards the central Arctic and finally exported from the Arctic via the Fram Strait. The second region is located north of Greenland and the Canadian Arctic Archipelago, with thick ice all through the year. The regions are illustrated in Figure 11.

6.1.1 Laptev Sea ice cover

Local ice production and export. The average seasonal cycle of sea ice area coverage in the Laptev Sea region is shown as the red lines in Figure 12. The annual cycle is relatively similar in the four simulations, with slight differences in summer, where the $N = 5$ and $N = 10$ simulations have a lower ice coverage at the beginning of the melt season, due to melting of the thinner ice categories. However, later in the year when the ice coverage is at its lowest, the simulations with more ice categories usually have a higher sea ice coverage. In winter all simulations are similar, when the ice covers the entire Laptev Sea region.

The average sea-ice thickness (thickness of sea ice, not including open water) is shown in Figure 12. The mean ice thickness has a much stronger sensitivity to the number of categories in the ice model. The simulations with $N = 5$ and $N = 10$ categories are similar, whereas the $N = 1$ and $N = 2$ simulations have a lower ice thickness. All simulations, however, show a similar seasonal cycle when one removes the annual average ice thickness. All experiments have a maximum ice thickness around July, with a local maximum just before October. The July maximum is presumably due to thin ice melting away, leaving thicker multi-year ice to dominate the area coverage. The sharp decline of ice thickness in October is due to freeze-up when new thin ice is created. All experiments show a minimum ice thickness in late October.

A possible reason for the more or less constant difference in ice thickness between the experiments can be the export of sea ice out of the Laptev Sea region. For instance, if the export is much higher in some of the experiments, the export of thick ice in winter is subsequently replaced by newly frozen ice. This will inevitably lead to thinner ice in the Laptev Sea region. The area export of sea ice, given as

$$T_A(t) = \int\int c_i \nabla \cdot \boldsymbol{v}_i \mathrm{d}\Omega_L \tag{69}$$

is shown in Figure 12. The area export of sea ice is highest in the experiments with a small number of categories, due to the lower average thickness and associated lower ice strength.

The area export differences between the experiments is a substantial factor concerning the ice thickness differences between the simulations. As the area export mainly occurs in winter, it means that newly frozen thin ice replaces thicker ice in the area, an effect which reduces the ice thickness in the area. The area export in winter is highest for the experiments with few categories, contributing the lowest ice thickness for these experiments.

The area export of sea ice out of the Laptev Sea region indicates how much open water is created within the region. Since the wintertime heat fluxes over open water are usually a lot higher than over ice, this export is important for the thermodynamic budget of the region. By this reasoning, one may expect an increased ice production in the experiments with few ice thickness categories. However, as demonstrated in Figure 12, this is not the case; the total growth of sea ice is highest in the experiments with $N = 5$ and $N = 10$ ice categories, especially in winter. This comes in spite of the higher ice thickness and lower open-water creation in these experiments.

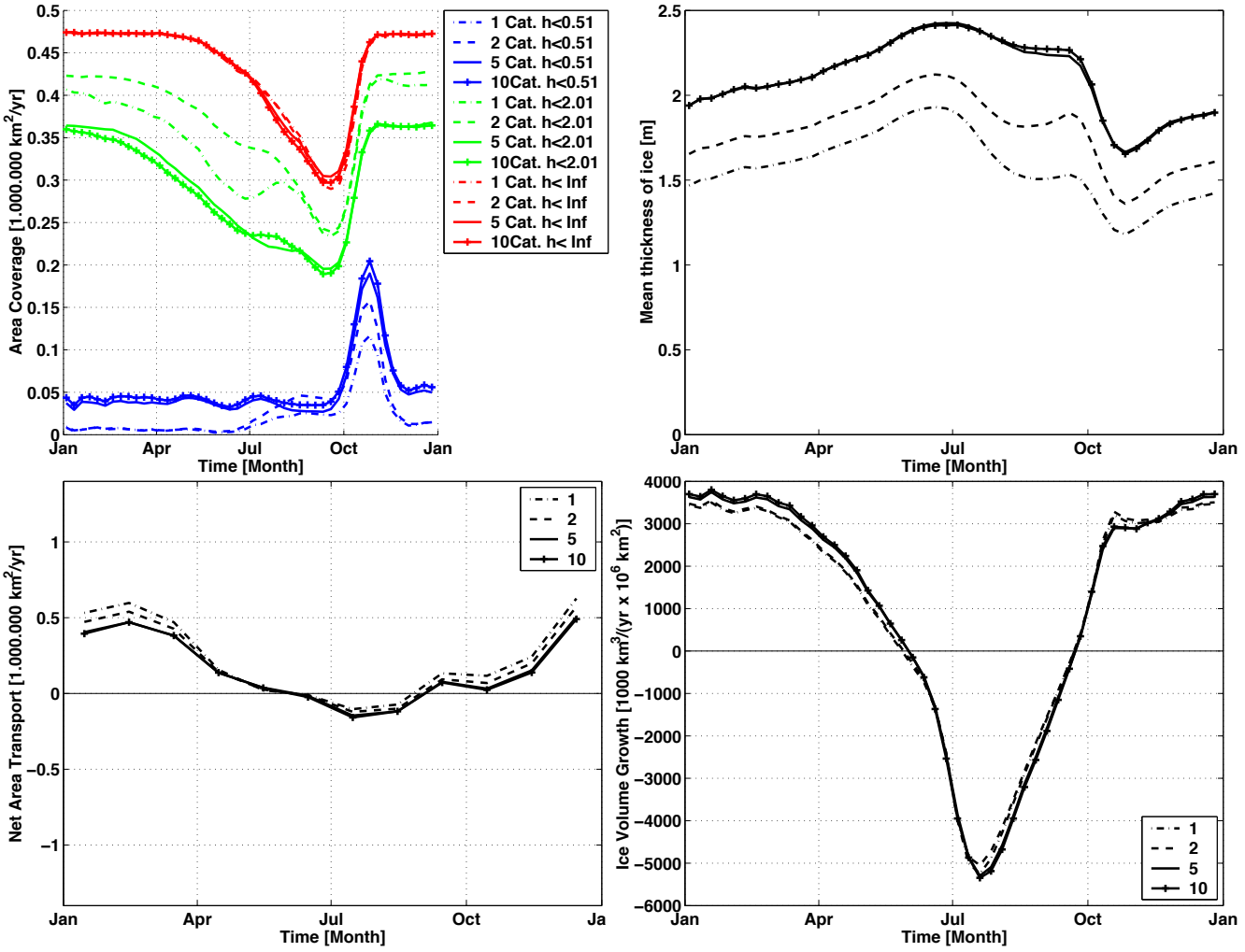

Figure 12: All figures are for the Laptev Sea region in Figure 11. Upper left - Area coverage of ice. Shown is the area covered by ice thicker than 0m, and less than the thickness indicated (< 0.5m - blue, < 2.0m - green, $< \infty$ - red), for the different category experiments($N = 1, 2, 5, 10$). Upper right - Mean ice thickness (not including open water). Lower left - Mean area export out the region. Lower right - Total ice volume growth in the Laptev Sea.

Cumulative distribution The average annual cycle of the cumulative ice thickness coverage in the Laptev Sea is illustrated in Figure 12. The figure shows the cumulative area coverage of ice thickness in the ranges $0 - 0.5$ m, $0 - 2.0$ m and $0 - \infty$ m. The figure indicates a convergence as the number of ice categories increase, illustrated by the similarity of the $N = 5$ and $N = 10$ experiments.

Figure 12 illustrates how there are substantial changes in the ice coverage of the region as the number of ice categories change. The most consistent change occurs for the thinnest ice coverage, where $0\,\text{m} < h < 0.5\,\text{m}$. As the resolution of the thinnest ice categories improve, there is an increase of the areal coverage of ice in this thickness range. This effect is strongest in winter, when there is virtually no ice in this thickness range for the $N = 1$ and $N = 2$ experiments. Experiments $N = 5$ and $N = 10$, on the other hand, retain this thin ice in winter.

The reason for the increase of ice in the $0\,\text{m} < h < 0.5\,\text{m}$ range stems from the treatment of newly frozen ice. This ice is added to one of the ice thickness categories described by the model. For instance, in the $N = 1$ case, newly frozen ice will be added to an already relatively thick ice category in a grid cell. This reduces the ice thickness of that category, but not enough for the ice thickness to become less than 0.5 m. If the thin ice is better resolved, as in the cases with $N = 5$ and $N = 10$, newly frozen ice will be added to an ice category which is already thin, and this ensures that the model actually describes this low, but important, fraction of the total ice cover. The Laptev Sea

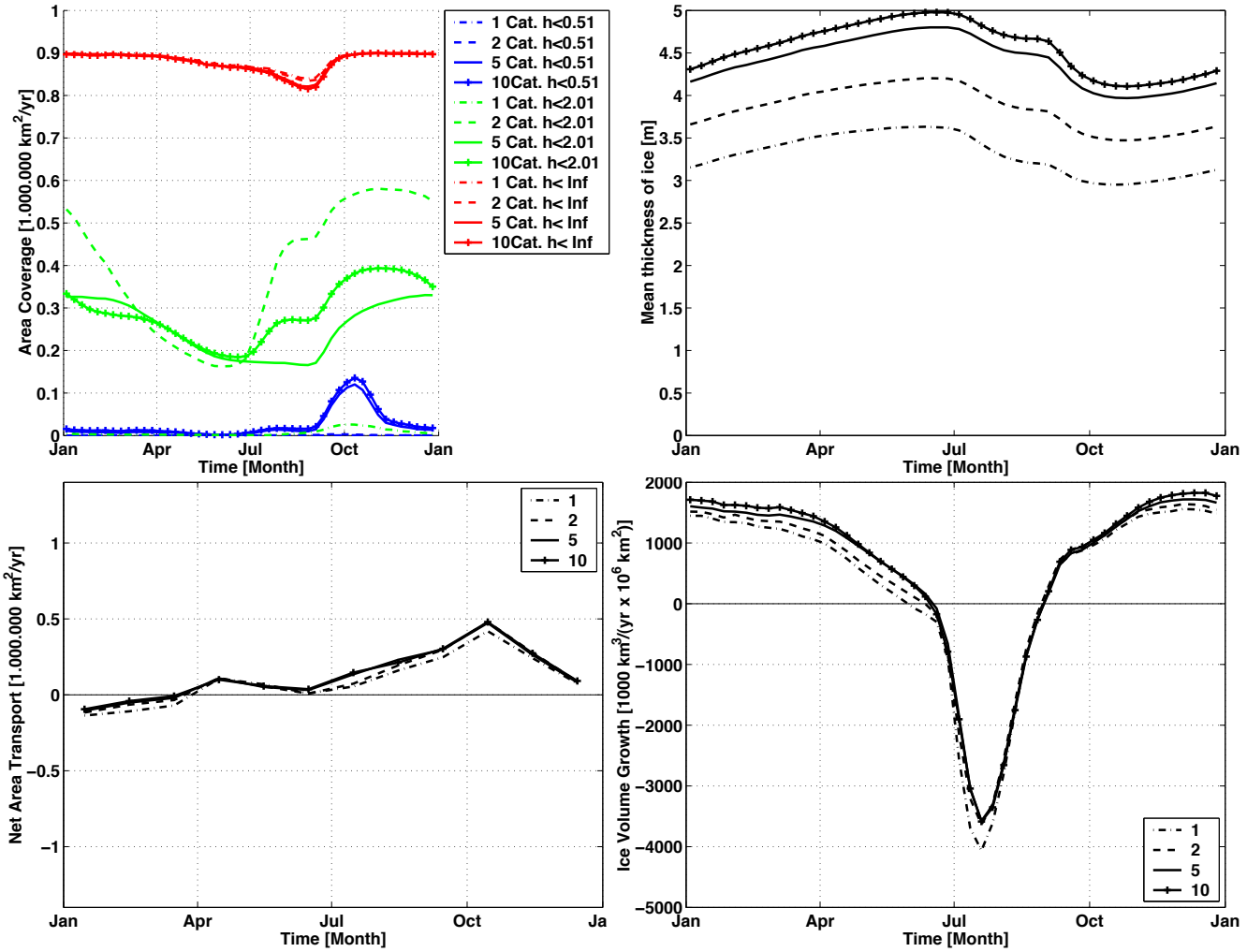

Figure 13: As Figure 12, but for the region North of Greenland.

region is usually a net exporter of sea ice in winter, see Figure 12, so the divergence causes new ice to be created in this region, making proper description of the thin end of the ice distribution vital.

The fractional coverage of ice thinner than 2m in the Laptev Sea region is slightly higher in the $N = 1$ and $N = 2$ experiments, an effect which is due to newly frozen ice reducing the thickness of already thick sea ice. For the total coverage of sea ice in the Laptev Sea, the different models are similar. This is because the tendency of $N = 5$ and $N = 10$ experiments to have higher bottom ablation in early spring (due to faster meltback of thin ice) is eventually offset by the higher average ice thickness in these experiments, reducing meltback in late summer.

6.1.2 Sea ice cover north of Greenland

The region North of Greenland is different from the Laptev Sea region when it comes to sea ice properties. First of all, this region usually has a lot higher coverage of thick multi-year ice than in the Laptev Sea region, which can be seen from Figures 13 and 13. Secondly, the net area export of sea ice is lower in winter than for the Laptev Sea region, Figure 13. In the period from December until April, the net area export out of the Greenland Sea region is close to zero for all experiments. It should be noted, however, that ice is exported out of the region in the western part of the section, due to the Beaufort Gyre, and into the region at its central/eastern part, due to the transpolar drift stream.

The low net area export in winter results in much lower open water creation when compared to the Laptev Sea. This is seen in Figure 13, where the fraction of ice thinner than 0.5 m is very low throughout winter, for all experiments. However, the fraction is still higher in the experiments with

a high number of categories, which is important due to the larger heat fluxes over thin ice. The time when the maximum fraction of this ice is present, is around October, when freeze-up starts.

It is noteworthy that only the experiments with $N = 5$ and $N = 10$ show any sign of this freeze-up process. For the other experiments, the pre-existing ice in a grid cell is so thick that the newly frozen ice does not reduce the thickness of ice categories to below 0.5 m, at least not to a significant degree. The situation is worst for the one-category simulation, where the freeze-up barely affects the area coverage of ice thicker than 2 m. On the other hand, all other experiments show an increase of ice thinner than 2 m during freeze-up.

Concerning the total ice cover, the experiments with five and ten ice thickness categories this time has a lower total area coverage in summer. This is likely due to the increased meltback of thinner ice which is described by these experiments. The experiments with one or two categories has so thick ice in the respective categories, that the melting in summer has a much lower influence on the total ice coverage.

The total growth of ice over a mean season is shown in Figure 13. The growth is given per unit area and can be compared with the corresponding Figure 12. As expected, the ice growth in this region is less than the growth for the Laptev Sea area, approximately half the value per unit area. The difference is due to the much lower export of ice, and corresponding lower heat fluxes over open water. In addition, the thicker ice in the Greenland Sea area has a stronger insulating effect, thereby reducing the ice growth.

It is interesting to see how large the differences are in the ice thickness between the different experiments, especially in winter. The increasing ice From our experience this is to a large extent due to the higher net heat fluxes which occur when we increase the number of ice categories, an effect already emphasized for thin ice by Maykut (1982). In fact, looking only at bottom freezing under ice (not shown), a similar pattern is seen, where better resolution of the ice thickness distribution leads to more freezing in winter. We will discuss this further in a idealized setting in Section 7.

6.2 Comparison with ULS data

As shown in the previous section, the simulations with a lower number of categories in general show a lower ice thickness. It is interesting to see how the model simulations compare to the Upward Looking Sonar(ULS) measurements undertaken by British and US submarines. These submarines measured the draft of the sea ice, and the data are available from the National Snow and Ice Data Center (NSIDC, *http://nsidc.org*) from the 1970s until the 1990s.

To compare the model output with the ULS data, the ice and snow thickness from the model is converted into ice draft,

$$\overline{h}_f = \frac{\rho_i \overline{h} + \rho_s \overline{h}_s}{\rho_w}, \tag{70}$$

where $\overline{h}$ and $\overline{h}_s$ are the mean ice and snow thickness, respectively, including open water. These model values are then compared to the averaged draft measurements from sonar. The average is calculated from the model and ULS data over cruise sub-sections typically of 50 km length. This length simply corresponds to the amount of data in each file available for the different cruises. For some of the datasets the comparison is done over shorter distances, for instance the SCICEX cruises use 12 km sections.

A plot of observations and model drafts for a section undertaken in 1994 is shown in Figure 14. The location of the different sub-sections (numbers on abscissa in Figure 14) is shown in Figure 14. The figure again illustrates how the increasing number of ice categories increases the ice thickness in the model. The $N = 5$ and $N = 10$ experiments have a slight positive bias, whereas the $N = 1$ and $N = 2$ have a negative bias in this situation. The ice draft in the experiment where $N = 5$ is shown in Figure 14. The cruise goes parallel to the coast line north of Greenland and the Arctic Archipelago, where it skims the thicker ice in this area. The cruise then moves into a region with thinner ice

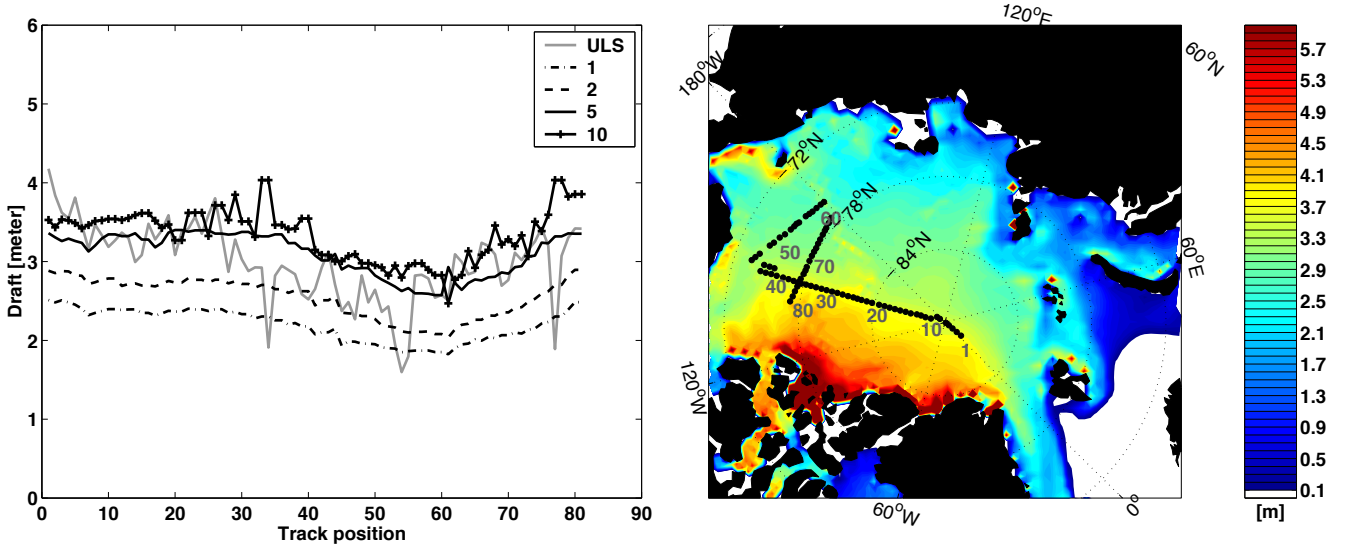

Figure 14: Left panel shows the drafts from observations and experiments in 1994, the right panel shows the positions of the individual sub-sections, background is average draft from the experiment with five ice thickness categories.

in the Chukchi Sea before it heads back towards the Canadian Archipelago. The large-scale spatial variation is well represented in all the simulations, but with different mean ice thickness.

The comparison in 1994 is relatively good, but other cruise tracks do not show the same correspondence. Taking each of the submarine cruise data sets available from NSIDC and computing the RMS error and bias of the model experiments, we arrive at Figures 15 and 15. The RMS errors for the different sections are usually higher in the cases with a low number of ice categories ($N = 1$ and $N = 2$), as illustrated in Figure 15. In particular the cruises "1986b", "1987", "UK87", "1988b", "UK87", "UK91" and "grayling92" stand out as cruises where the low-category simulations have large errors. A large part of this RMS error stems from a negative bias in the $N = 1$ and $N = 2$ simulations, seen in Figure 15. The exception is the "UK87" cruise which does not show a large bias for the $N = 1$ and $N = 2$ simulations. This cruise does in stead show a very high small scale variability which is hard to re-create in a coarse-resolution model.

The bias in Figure 15 shows a consistent picture with increasing bias for increasing number of ice categories. This is consistent with what we found in the regional analysis for the Laptev Sea and the Greenland region. It also shows a picture of an ice thickness increase with the number of categories which is quite consistent in space and time. Looking at the bias it appears that the experiment with $N = 5$ has the lowest overall magnitude of the bias, with strong underestimate of the ice thickness in experiments $N = 1$ and $N = 2$, and $N = 10$ estimating slightly thicker ice.

The comparisons further illustrate how important the number of ice thickness categories are when it comes to modeling the ice mass balance in the Arctic. In the next section we will examine a key mechanism causing this, by looking at the conducive heat fluxes through the ice in one vs. two-category sea-ice models.

6.3 Comparison with SSM/I data

The SSM/I data set can be used to calculate how much of the surface area of the ocean is covered by sea-ice. Such a comparison is done in Figure 16, showing the 70% ice concentration from observations (grey) and model (black). The ice concentration from the SSM/I data was calculated using the NORSEX algorithm (Svendsen et al., 1983). The ice concentration in the simulations over-estimate the actual ice cover and sea-ice extent. There are some factors which partly explain this overestimate.

First of all, the ocean model is relatively coarse, a property that frequently causes a too low

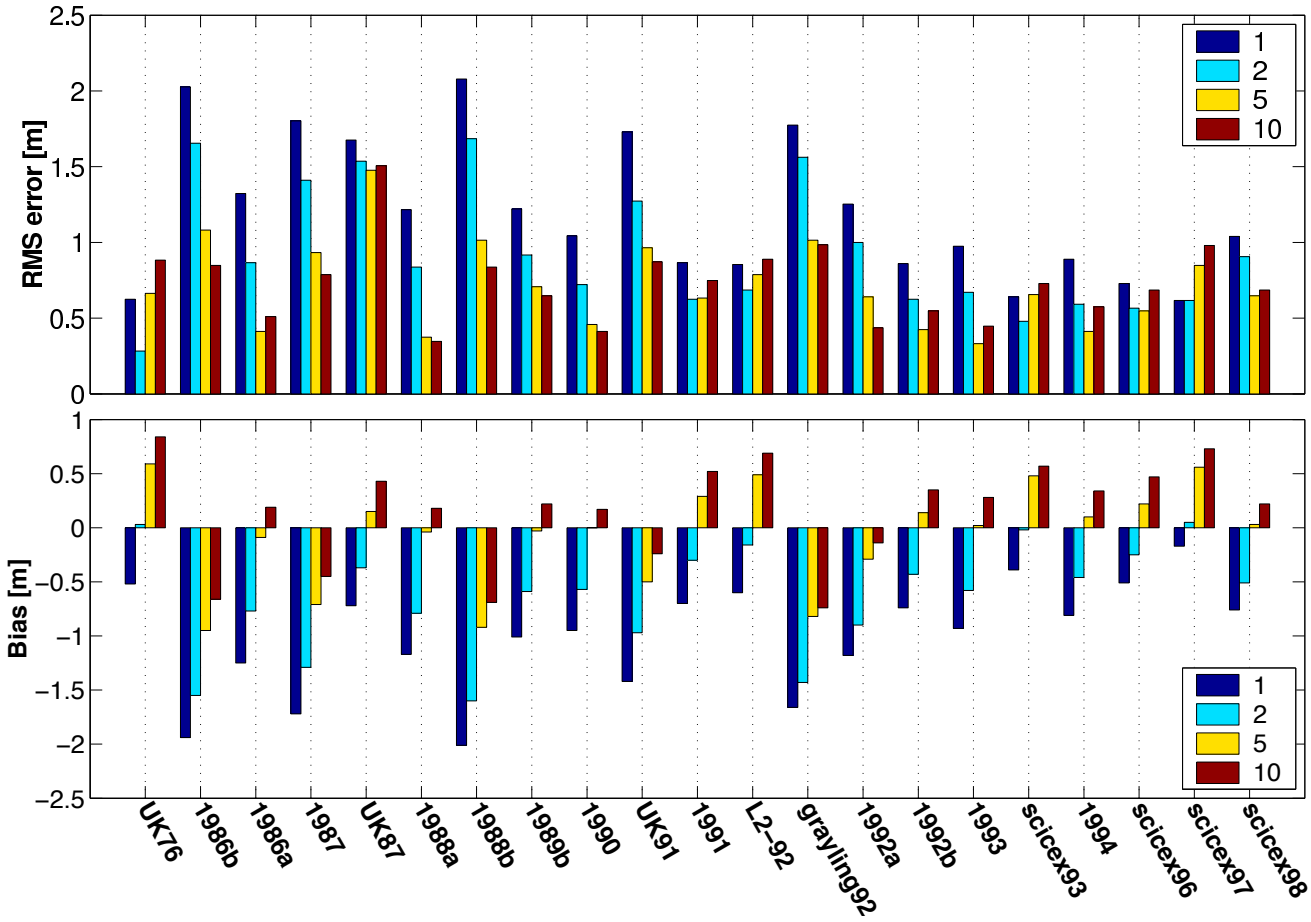

Figure 15: The upper panel shows the RMS errors of the drafts from the different experiments, compared against the ULS data. The lower panel shows the bias.

transport of warm water transported from the North Atlantic into the Nordic Seas. This explain at least some of the overestimated ice cover in the Greenland and Barents Sea in winter. Also, when comparing the model results with this data set, it should be kept in mind that lateral melting was ignored in the model simulations. The sea ice model used in this study is of a similar type as that used by Bitz et al. (2001), but we have neglected the lateral melt parameterization commonly used by other sea ice models. Many lateral melt parameterizations, for instance the one by Häkkinen and Mellor (1992), exist primarily to describe how the thin end of the ice distribution melts away faster than the thick end. In other words, they do not actually describe lateral melting. Lateral melting is an important process in the Arctic, but Steele (1992) find it is primarily important for smaller sized ice floes, and not that important in the central ice pack. However, the sea ice in the marginal ice zone is very often severely broken up, and lateral melt parameterizations should probably used as well in these regions. Including such a parameterization might improve the model simulations.

In the simulations we chose to leave lateral melt parameterizations out, to examine the effect of resolving the ice thickness distribution, wherein melting of the thin ice is an important effect. Note, however, that including this effect would not explain the increased ice thickness seen with increasing categories. This effect would only be used in the $N = 1$ and $N = 2$ experiments, since they do not resolve the thin ice. Using the lateral melt in these experiments should lead to a further decreased ice thickness.

7 Discussion

We will look closer at one of the thermodynamic processes which is important for the ice mass balance, that of wintertime freezing at the bottom of the ice. Assuming that the ocean temperature

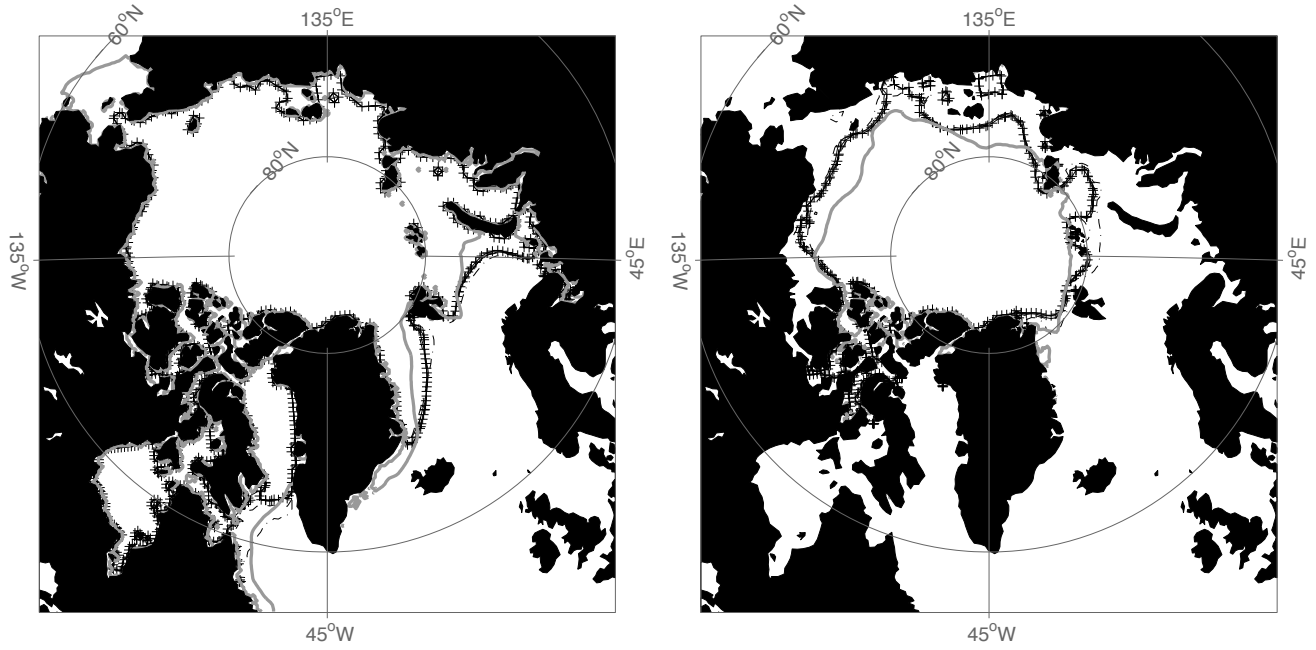

(a) (b)

Figure 16: Average 70% Sea ice concentration contour, for the time period 1979–2001. Left: March, Right: September. The grey line indicates SSM/I estimates, the dashed line is for the experiment with $N = 1$ category, solid black line and solid black line with '+' signs is for the $N = 5$ and $N = 10$ experiments, respectively.

is at the freezing point, the conductive heat fluxes here are the most important for determining the wintertime freezing rates. We will proceed to discuss these fluxes in idealized circumstances. First by looking at the conductive heat flux dependency on ice thickness and atmospheric influence, using a single ice category. We will then use the results to discuss the effective conductive heat flux for an ice cover consisting of two discrete ice thicknesses. It will be shown how the heat flux is always larger in the two-category solution. These findings will then be compared to results from the coupled model.

7.1 Conductive heat flux dependency on ice thickness

The conductive heat flux is important for the freezing rates at the bottom of the ice, and its dependence on ice thickness is studied here in a simplified setting. It is assumed that the conductive heat flux to the top surface of the ice is balanced by the longwave heat flux from the surface. All other heat flux components involved in the surface heat flux budget are ignored for simplicity. Another assumption is that the steady state solution of the heat equation is valid, so the conductive heat flux can be described by Eq. (4). The cloud cover is 0.5, the air temperature is $-30°$C, and the bottom surface of the ice is fixed at a temperature of $-1.8°$C. The snow cover on top of the ice is assumed to be 0.1 m. Using these assumptions, equations (86) and (4) are solved to find the conductive heat flux through ice of thickness h. The conductive heat flux dependence on the ice thickness h is given as the solid line in Figure 17. Note that for very thin ice, the snow cover on top would become snow-ice, which is not accounted for here.

Figure 17 shows the conductive heat flux with a snow cover of 0.1 m for all ice thicknesses. However, it could be argued that thinner ice has thinner snow cover than thicker ice. To examine this, the equations can be solved for a snow thickness which varies linearly with ice thickness. Letting $h_s = \frac{1}{20}h$ gives a snow thickness of 0 m for $h = 0$ and 0.3 m when $h = 6$ m. The corresponding conductive heat flux for is given as the the dashed line in Figure 17. The disappearing snow thickness drastically increase the conductive heat flux when h is low, whereas for high h the insulating properties of the

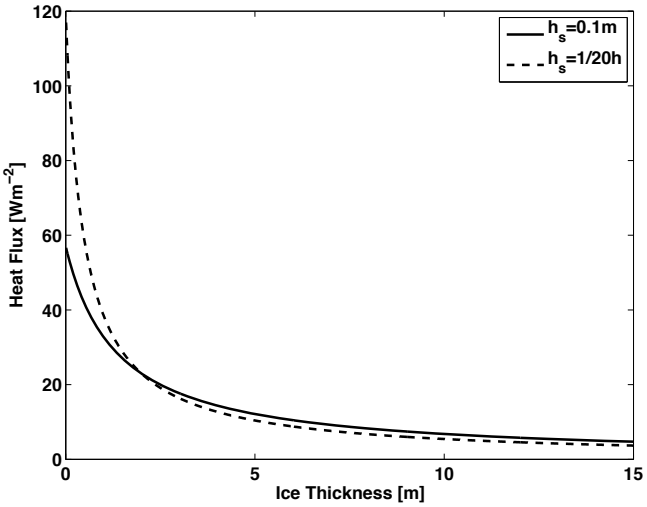

Figure 17: The figure shows the heat flux through the ice when assuming uniform snow cover of 0.2 m (solid) and a linear dependence to ice thickness where $h_s = h/20$.

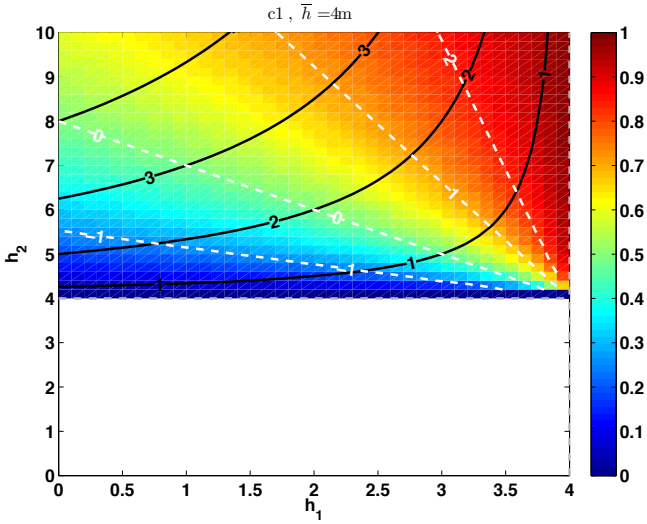

Figure 18: The figure shows the value of c_1 when varying the ice thickness values in the two categories (h_1 and h_2), assuming a mean ice thickness of $\overline{h} = 4\,\mathrm{m}$, and a fully ice-covered ocean ($c_1 + c_2 = 1$).

thicker snow cover lowers the conductive heat flux. Note that as $h \to 0$ the solution becomes increasingly incorrect, as other heat fluxes, such as latent heat released by freezing ice, must be considered as well.

The preceding cases are for a situation where longwave heat loss from the ice surface is the only atmospheric forcing. In a more general situation, the net atmospheric heat flux can be approximated as a linear function of surface temperature, while the conductive heat flux is still approximated by Eq. (4). The balance between conductive and atmospheric heat fluxes at the surface then becomes

$$-k_{\mathrm{eff}} \frac{T_{\mathrm{srf}} - T_0}{h + h_s} = a + bT_{\mathrm{srf}}\,, \tag{71}$$

where k_{eff} is given as in Eq. (5), and $b > 0$. This equation can be solved for T_{srf}, which, when inserted into the conductive heat flux equation gives the following form of the heat flux dependency on h:

$$F_c(h) = \frac{k_s k_i \left(a + bT_0\right)}{k_s k_i + b\left(hk_s + h_s k_i\right)}\,. \tag{72}$$

Neglecting snow thickness, Equation (72) is asymptotically proportional to $\frac{1}{h}$, just as the example plots in Figure 17. This behavior is important since the analysis of the case with longwave forcing will be similar to cases with several forcing components together, e.g. latent, and short wave heat fluxes as well.

7.2 Extension to a situation with two ice categories

Figure 17 indicates the expected conductive heat flux as the mean ice thickness varies for a single ice category model. For a multi-category ice model, the effective conductive heat flux, summed up over all categories, will change because different ice thicknesses are resolved. The effect of this is explored by looking at the changes introduced when moving to a simple two-category description of the ice. The mean ice thickness is fixed to 4 m, and the heat fluxes under for partitionings of the ice cover is considered.

In the following we look at a region completely covered with ice, with an ice thickness distribution given as $g(h)$. For a single category ice thickness model, the ice thickness of the category would be the mean ice thickness. The same region can be described by a two-category ice thickness distribution. Let the threshold limit ice thickness separating the categories be h_c. In this case, the average ice thickness can be written

$$\overline{h} = h_1 c_1 + h_2 c_2 \,, \tag{73}$$

where c_1, h_1 is the concentration and average ice thickness over the interval $(0, h_c)$ and c_2, h_2 is the concentration and average ice thickness over the interval (h_c, ∞). We also need to have

$$c_1 + c_2 = 1 \,. \tag{74}$$

For simplicity, assume $h_c = \overline{h}$, so that $h_1 < \overline{h} < h_2$ when $c_1, c_2 > 0$. Equations (73) and (74), rewritten in terms of the ice thickness values give

$$c_1 = \frac{h_2 - \overline{h}}{h_2 - h_1} \,, \qquad\qquad c_2 = \frac{\overline{h} - h_1}{h_2 - h_1} \,. \tag{75}$$

The solution of c_1 as h_1 and h_2 vary is illustrated in Figure 18. The limiting cases as $h_2 \to \overline{h}$ and $h_1 \to \overline{h}$ lead to the disappearance of one of the terms c_1 or c_2, a solution which is equivalent to the single ice category solution with $c = 1$ and $\overline{h} = 4$m.

The effective heat flux, $F_c^\star$, through the two-category ice cover is given as

$$F_c^\star \left(h_1, h_2; \overline{h}\right) = c_1 F_c(h_1) + c_2 F_c(h_2) \,. \tag{76}$$

Using Equation (75), the partial derivatives (wrt. h_1 and h_2) of this function become

$$\frac{\partial F_c^\star}{\partial h_1} = \frac{h_2 - \overline{h}}{h_2 - h_1} \left(F_c'(h_1) - \frac{F_c(h_2) - F_c(h_1)}{h_2 - h_1} \right) \,, \tag{77}$$

$$\frac{\partial F_c^\star}{\partial h_2} = \frac{\overline{h} - h_1}{h_2 - h_1} \left(F_c'(h_2) + \frac{F_c(h_2) - F_c(h_1)}{h_2 - h_1} \right) \,. \tag{78}$$

Using the Mean Value Theorem, we have

$$\frac{\partial F_c^\star}{\partial h_1} = \frac{h_2 - \overline{h}}{h_2 - h_1} \left(F_c'(h_1) - F_c'(h_\star) \right) \,, \tag{79}$$

$$\frac{\partial F_c^\star}{\partial h_2} = \frac{\overline{h} - h_1}{h_2 - h_1} \left(F_c'(h_2) - F_c'(h_\dagger) \right) \,, \tag{80}$$

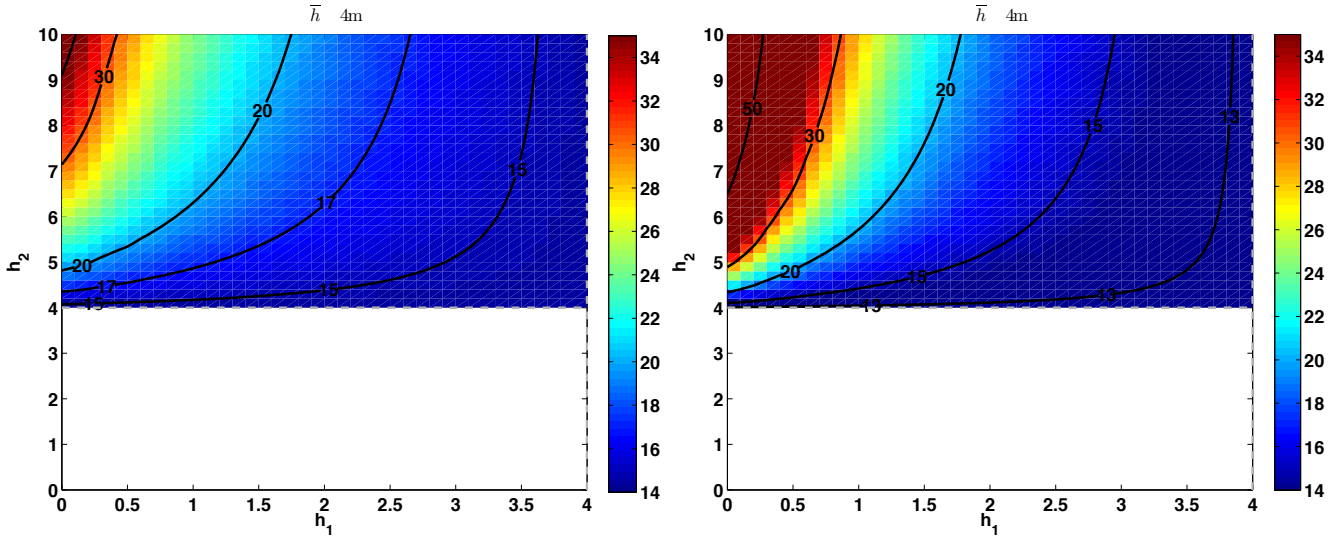

Figure 19: Illustration of the effective heat flux through a two-category ice cover as h_1 and h_2 varies (see text). The left panel shows the heat fluxes when using heat flux dependency on h as in the solid line in Figure 17. The right panel shows the heat fluxes when using heat flux dependency on h as in the dashed line in Figure 17.

where $h_1 \leq h_\star \leq h_2$ and $h_1 \leq h_\dagger \leq h_2$. Note that for $F_c(h)$ as shown in Figure 17, the second derivative is positive. For the general form given by Eq. (72), it can be shown that the second derivative is positive as long as $h_s''(h) \leq 0$, with the restriction that $h_s(h)$ is positive. This results in

$$F_c'(h_1) \leq F_c'(h_\star) \leq F_c'(h_2)\,, \text{ and } F_c'(h_1) \leq F_c'(h_\dagger) \leq F_c'(h_2)\,. \tag{81}$$

This last equation, in conjunction with equations (79) and (80), gives the following constraints for the derivatives when $h_1 \leq \overline{h}$ and $h_2 \geq \overline{h}$

$$\frac{\partial F_c^\star}{\partial h_1} \leq 0 \qquad\qquad \frac{\partial F_c^\star}{\partial h_2} \geq 0\,. \tag{82}$$

which places the minimum value of $F_c^\star$ on the boundaries $h_1 = \overline{h}$ and $h_2 = \overline{h}$. As mentioned earlier, these solutions are all equivalent to a single ice category description of the conductive heat flux. This means that for a conductive heat flux dependency on ice thickness of the same form as in Figure 17, or of the form given by Eq. (72), the conductive heat flux through the ice cover is consistently underestimated when using a single ice category, as compared to a two-category description. In fact, any heat flux whose dependence on ice thickness satisfies $F_c''(h) > 0$, will lead to the same conclusion.

Illustrations of the effective heat flux through a "two-category" ice cover are shown in Figure 19, as h_1 and h_2 vary. The left panel show the result when applying the conductive heat flux corresponding to the solid line (fixed snow thickness) in Figure 17, and the right panel shows the result when applying the conductive heat flux corresponding to the dashed line (varying snow thickness) in Figure 17. The most nonlinear heat flux dependence on h (as given by the second derivative) shows a greater span of values, as expected from equations (79) and (80).

Figure 19 illustrate how the single ice-category solution (on the boundaries $h_1 = 4$m and $h_2 = 4$m) always underestimate the possible two ice-category solutions having the same average ice thickness. The greatest span of values occur when $h_1 < 0.8$m, to be expected given the high heat fluxes for thin ice, and the results of Maykut (1982). Nonetheless, there is still a significant variation for $h_1 > 0.8$m. Using the heat flux where snow thickness varies with ice thickness, the one category solution gives $\approx 13\mathrm{W\,m^{-2}}$, whereas the two-category solution with $h_1 = 1$m and $h_2 = 6$m yields $\approx 20\mathrm{W\,m^{-2}}$.

It is important to realize that it is the nonlinearity of the heat flux which causes the total heat flux to increase with more ice categories. For instance, consider an artificial conductive heat flux

which varies linearly from a value of $60\mathrm{W\,m^{-2}}$ for $h = 0\,\mathrm{m}$ to zero for $h = 8\,\mathrm{m}$. For a two-category ice description having $\overline{h} = 4\,\mathrm{m}$, the total heat flux for this case will be exactly equal to the single ice category solution, since for $0\mathrm{m} < h_1 < h_2 < 8\mathrm{m}$, Equations (79) and (80) give

$$\frac{\partial F_c^\star}{\partial h_1} = 0 \qquad\qquad \frac{\partial F_c^\star}{\partial h_2} = 0\,. \tag{83}$$

The preceding argument can be further extended to having more than two ice categories, by sub-dividing the categories into smaller parts. In other words, the more ice categories are introduced in this way, the higher the effective conductive heat flux will become, converging towards an upper limit.

7.3 Effects on the ice mass balance

As illustrated, a better resolved ice thickness distribution leads to an increased growth rate in winter. Ice properties and snow cover may change this, but as a general rule we expect the findings in the last section to be true. What is the effect of the increased growth rate on the regional and global ice mass? The answer depends on the effect the better resolved ice thickness distribution has on summertime melting. Given that a better resolved ice thickness distribution also allows the thin ice to melt away earlier than in a one-category model, it is possible that a well-resolved ice thickness distribution also ends up with a higher melt during summer, primarily through heat absorbed in a higher open-water fraction, followed by bottom ablation. The increased melting in summer could outweigh the increased freezing in winter. The balance between these effects will also be different between seasonal and perennial ice-covered seas.

However, the experiences from the coupled model indicate that as the number of categories increase, the summertime melting does not outweigh the increased freezing in winter. In the Laptev Sea, for instance, the summertime melt due to an increased open-water fraction is higher in the experiments with $N = 5$ and $N = 10$ categories, yet not enough to overcome the increased freezing in winter, relative to the $N = 1$ and $N = 2$ experiments.

The suggested mechanism for the increased ice thickness with an increasing number of categories in the experiments is therefore as follows; Additional ice categories lead to an increased wintertime conductive heat flux through the ice cover, and increased ice formation. As summertime melt starts, initially the lateral melting is increased with more ice categories, due to thin ice melting away. However, as the mean ice thickness of the experiments with more ice categories is higher, the overall summertime melting does not vary much between the experiments. This is because thick ice persists longer in the experiments with more categories, apparently preventing some of the sea-ice albedo feedback one might expect. An equilibrium ice thickness for any given experiment is reached at the time when the ice is thick enough such that wintertime freezing balances the summertime melting. Due the effects mentioned above, this equilibrium thickness is higher in the experiments with more ice categories.

It is interesting to compare our results to those of Bitz et al. (2001), who use a very similar sea ice model formulation. Their result are similar to ours, with an ice thickness increasing with the number of ice categories, a result also supported in the experiments by Schramm et al. (1997). In Bitz et al. (2001), the ice coverage on the Arctic shelves and in the Arctic Ocean do exhibit some variability across their experiments but, as in our case, there is no clear-cut correspondence between the number of categories, and the total ice coverage in the region. There is however, a clear convergence towards their 15 ice category solution, and towards an upper ice thickness limit with increasing N.

The effect of resolving the thin end of the ice thickness distribution has been well known in sensitivity experiments for multi-category models, the findings shown here should serve as a supplement to this. We have illustrated how any sub-division of the ice thickness distribution into categories increases the heat flux, not only for the thin end of the ice thickness distribution, but everywhere. Depending on the atmospheric forcing, and the nonlinearity of the heat flux with h, the division of ice thicker than 1 m into categories can also have a large effect on the effective conductive heat flux.

8 Conclusion

This work has discussed the implementation of a thermodynamic and kinematic model component of a sea-ice model. The ice dynamics are not covered by the model described here, so the implementation with the HYCOM ocean model uses the EVP sea ice dynamics component to calculate the ice drift.

The implementation uses the theory of Thorndike et al. (1975) to describe the ice cover. This involves the description of the ice thickness distribution, as well as the description of ridging and rafting processes which tend to modify the ice thickness distribution. Also presented are the heat fluxes and the treatment of conductive heat flux in the ice.

The ice thickness distribution used in this model is described mathematically using delta-functions, and a presentation of the method used and constraints put on the ice thickness distribution is given. This involves steps needed to limit the number of delta-functions used to describe the ice thickness distribution, as well as steps for changing the thermodynamical properties of the ice model when the associated ice thickness grows beyond specified limits (limits which define the ice classes in our model).

The performance of the model is assessed in a model coupled with the HYCOM ocean model and the EVP sea ice rheology model, run with ERA40 forcing. The comparison with submarine ULS data shows that the sea ice model gives realistic sea ice thickness fields. The model is also able to produce a reasonable ice transport out of Fram Strait, although the volume transport is underestimated, likely due to too low drift rates in the model.

As set up in the coupled model run with HYCOM and EVP, the model has five thickness classes. This can quite easily be changed in the model, and an increased number of ice classes will probably improve the results presented here. For instance, it might be beneficial to add more ice classes to the thin end of the thickness space in order to better model ice rafting, or ice classes can be added to the thick end of the thickness space, allowing better simulation of pressure ridges in the ice. To model Antarctic sea-ice it will also be beneficial to have more ice classes describing thin ice, as this ice is thinner and of a more seasonal character than Arctic sea ice. In the end, the choice of ice classes will be a trade-off between the resolution of the sea ice thickness space and computational efficiency.

A Heat fluxes

A.1 Atmospheric and oceanic heat fluxes

The latent ($F_{\mathrm{e,srf}}$), sensible ($F_{\mathrm{s,srf}}$), long wave ($F_{\mathrm{L,srf}}$) and short wave ($F_{\mathrm{r,srf}}$) heat fluxes at the surface are given as:

$$F_{\mathrm{e,srf}} = C_E \rho_a L_{\mathrm{srf}} \|\boldsymbol{u}_a\| \left(q^{\star}_{\mathrm{srf}} - q_a\right) \tag{84}$$

$$F_{\mathrm{s,srf}} = C_H \rho_a c_{\mathrm{pa}} \|\boldsymbol{u}_a\| \left(T_{\mathrm{srf}} - T_a\right) \tag{85}$$

$$F_{\mathrm{L,srf}} = 4\epsilon\sigma T_a^3 \left[T_{\mathrm{srf}} - (1 - \frac{f_{\mathrm{lw}}}{4})T_a\right] \tag{86}$$

$$F_{\mathrm{r,srf}} = -F_{\mathrm{r0}} \left(C\,\alpha^{\mathrm{dif}}_{\mathrm{srf}} - (1-C)\alpha^{\mathrm{dir}}_{\mathrm{srf}}\right) . \tag{87}$$

The subscript "srf" is used to indicate what the actual surface material is, ice (srf $= i$), snow (srf $= s$) or water (srf $= w$). Here $\boldsymbol{u}_a$ is the wind at 10 meters height, L_{srf} is the heat of condensation for a water surface, it is the heat of sublimation for a ice or snow surface. ρ_a is the air density and c_{pa} is the specific heat of air at constant pressure. Temperature (T) and specific humidity (q) are given at the surface (srf) or in the the atmospheric mixed layer (a). At the surface the air humidity is assumed to be saturated, denoted by the $\star$ superscript. The bulk transfer coefficients C_H and C_E are given in Table 2 in Isemer et al. (1989).

The net longwave flux at the surface, Equation (86), is based on Efimova (1961), as recommended by Budyko (1974). ϵ is the emissivity, set to the same value for ice, snow and water, and σ is the

Albedo	Description	Value
$\alpha^{\rm dir}_{\rm i,m}$	Direct albedo for melting ice ($T_i = T_m$)	0.62
$\alpha^{\rm dir}_{\rm i,d}$	Drect albedo for dry ice	0.73
$\alpha^{\rm dir}_{i}$	Thickness dependent albedo for dry ice	Equation (91)
$\alpha^{\rm dif}_{i}$	Diffuse albedo for ice	0
$\alpha^{\rm dir}_{\rm s,max}$	Maximum albedo for snow	0.81
$\alpha^{\rm dir}_{\rm s,min}$	Minimum albedo for snow	0.73
$\alpha^{\rm dif}_{s}$	Diffuse albedo for snow	0
$\alpha^{\rm dir}_{w}$	Direct albedo for water	Equation (90)
$\alpha^{\rm dif}_{w}$	Diffuse albedo for water	0.065

Table 4: List of albedo values used, number refers to equations which apply

Stefan-Boltzman constant. The coefficient $f_{\rm lw}$ is a correction factor (Budyko, 1974),

$$f_{\rm lw} = (0.254 - 4.95 \times 10^{-5} e_a) \times (1 - \chi\, C^{1.2})\,, \tag{88}$$

where e_a is the vapor pressure of the air and C is the total cloud cover fraction. The cloudiness exponent is taken from Budyko (1974) and Isemer et al. (1989). The parameter χ is a cloud correction factor, from Tab. 8 in Budyko (1974),

$$\chi = 0.5 + 0.246|\phi|\,, \tag{89}$$

where ϕ is the latitude, measured in radians.

The shortwave heat flux, $F_{\rm r,srf}$, is given by Equation (87). $F_{\rm r0}$ is the cloud–top insolation, and $\alpha^{\rm dir}_{\rm srf}$ and $\alpha^{\rm dif}_{\rm srf}$ are the direct and diffuse albedoes of the surface. The cloud top insolation is given as in Drange and Simonsen (1996). The different albedo values used are summarized in Table 4.

The diffusive albedo component over water is set to 0.065 following Payne (1972), while the direct component over water depends on the zenith angle θ_z (Roeckner et al., 1992)

$$\alpha^{\rm dir}_{w} = \max\left(0.15, \frac{0.05}{\cos\theta_z + 0.015}\right) \tag{90}$$

The albedo of ice depends on wether the surface is at the melting point or below. If it is at the melting point, the direct albedo is set to the value of $\alpha^{\rm dir}_{i,m}$, whereas if the surface is dry, it is set to $\alpha^{\rm dir}_{i,d}$, see Table 4. If the ice surface is dry and snow-free, we use the thin ice albedo parametrization of Maykut (1982), where the albedo will depend on the ice thickness:

$$\alpha^{\rm dir}_{\rm i,thin} = \min\left(\alpha^{\rm dir}_{i,d}, .08 + .44 h_i^{0.28}\right)\,. \tag{91}$$

The snow albedo is modeled by using parametrizations from Douville et al. (1995), incorporating effects due to snow aging, surface melt and precipitation. Snowfall increases the albedo of the surface towards the maximal snow albedo value, while rain, surface melt and snow aging decreases the albedo towards the minimal snow albedo value. The maximum and minimum albedo values for snow are given in Table 4.

The heat flux between the ocean mixed layer and the ice is from Holland and Jenkins (1999),

$$F_{\rm w} = -\rho_w c_{\rm pw} \gamma_T (T_f(S_w) - T_w)\,, \tag{92}$$

where ρ_w is the density of the underlying water, $c_{\rm pw}$ is the specific heat capacity of water, and γ_T is a heat exchange velocity. The temperature T_w is the temperature of the water and $T_f(S_w)$ is the temperature at the ice/ocean interface, assumed to be at the freezing point of seawater with salinity S_w. Note that the mixed layer temperature is not allowed to be lower than the freezing point, preventing supercooling of water and frazil ice formation, this gives a heat flux which can only melt the bottom of the ice. The exchange velocity γ_T is expressed as in the two–equation formulation of Holland and Jenkins (1999), where the salinity of water close to the ice/ocean interface is assumed to be the same as the salinity of the mixed layer.

A.2 Brine parametrization

When shortwave radiation meets the ice surface, an amount of the radiation will penetrate it. Some of this radiation will be absorbed by the ice, while some of the radiation may penetrate through the ice into the underlying ocean. The brine pockets serve as a storage of latent heat in the ice, which retards surface melting in spring, and retards freezing in fall. The parametrization of this effect is taken from Semtner Jr. (1976). The heat stored in the ice is given by Q_{brine}, and this heat storage has a maximum value $Q_{\text{brine}}^{\max}$ given as

$$Q_{\text{brine}}^{\max} = q_f L_{\text{i0}} \min(h_i, 1)\,, \tag{93}$$

where L_0 is the latent heat of ice, and q_f is a parameter giving the maximum heat stored in fraction of the total latent heat of the ice. If the heat storage is at maximum, the ice is considered opaque, and all shortwave radiation is retained at the surface.

The heat storage represents melted ice, so the heat of fusion of ice is adjusted to account for this. If there is heat in the brine store, the heat of fusion of the ice becomes

$$L_i = L_{\text{i0}} - \frac{Q_{\text{brine}}}{h_i}\,, \tag{94}$$

which ensures that heat is conserved when ice freezes or melts.

A.2.1 Penetrating shortwave radiation

The shortwave radiation penetrating the ice surface is

$$F_{\text{brine}}^{\text{in}} = F_{\text{r,srf}} I_0 \tag{95}$$

where I_0 denotes the fraction of the incoming radiation which penetrates the surface. I_0 is given as

$$I_0 = \begin{cases} f_i(h_i) & h_s = 0 \text{ and } Q_{\text{brine}} < Q_{\text{brine}}^{\max} \\ 0 & \text{otherwise} \end{cases} \qquad f_i(h_i) = \max(0.17, 1 - 8.3h_i) \tag{96}$$

The amount of shortwave radiation absorbed by the ice depends on how much of the shortwave radiation goes through the ice and into the underlying ocean. This is given by

$$F_{\text{rw}} = -e^{-1.5(\max(h_i - 0.1, 0))} F_{\text{brine}}^{\text{in}} \tag{97}$$

which means that the following amount of shortwave radiation is absorbed by the heat storage of the ice slab

$$\frac{\partial Q_{\text{brine}}}{\partial t} = -\left(F_{\text{brine}}^{\text{in}} - F_{\text{rw}}\right)\,. \tag{98}$$

A.2.2 Heat flux from the heat store

In fall, the brine parametrization serves to retard the fall freeze-up. This is accomplished by extracting heat from the brine heat reservoir when the surface temperature of the ice or snow is below the freezing point. That is, when the surface heat balance predicts a surface temperature below the melting point T_m, then heat is extracted from the brine reservoir to keep the surface temperature at the melting point T_m, giving a positive heat flux $F_{\text{brine}}^{\text{out}}$ on the surface. This heat flux is connected to the heat flux balance of the surface, and is be specified along with the ice surface heat budget in Section 2.2.1.

References

Bentsen, M., Evensen, G., Drange, H., Jenkins, A. D., 1999. Coordinate transform on a sphere using conformal mapping. Mon. Wea. Rev. 127, 2733–2740.

Bitz, C. M., Holland, M. M., Weaver, A. J., Eby, M., 2001. Simulating the ice-thickness distribution in a coupled climate model. J. Geophys. Res. 106 (C2), 2441–2461.

Bleck, R., 2002. An oceanic circulation model framed in hybrid isopycnic–cartesian coordinates. Ocean Modelling 1, 55–88.

Budyko, M. I., 1974. Climate and Life. Academic Press, New York.

Douville, H., Royer, J.-F., Mahfouf, J.-F., 1995. A new snow parametrization for the Météo France climate model, part I: validation in stand–alone experiments. Clim. Dyn. 12, 21–35.

Drange, H., Simonsen, K., 1996. Formulation of air-sea fluxes in ESOP2 version of MICOM. Tech. Rep. 125, Nansen Environmental and Remote Sensing Center, Bergen, Norway.

Efimova, N. A., 1961. On methods of calculating monthly values of long-wave radiation. Meteorol. Gidrol. 10, 28–33, mGA 13.9–523.

Häkkinen, S., Mellor, G. L., 1992. Modeling the seasonal variability of a coupled Arctic ice–ocean system. J. Geophys. Res. 97 (C12), 20285–20304.

Harvey, L. D. D., 1990. Testing alternative parametrizations of lateral melting and upward basal heat flux in a thermodynamic sea ice model. J. Geophys. Res. 95, 7359–7365.

Hibler III, W., 1980. Modeling a variable thickness sea ice cover. Monthly weather review 108 (12), 1943–1973.

Holland, D. M., Jenkins, A., 1999. Modelling thermodynamic ice-ocean interactions at the base of an ice shelf. J. Phys. Oceanogr. 29 (8), 1787–1800.

Hunke, E. C., Dukowicz, J. K., 1997. An elastic-viscous-plastic model for sea ice dynamics. J. Phys. Oceanogr. 27, 1849–1867.

Isemer, H. J., Willebrand, J., Hasse, L., 1989. Fine adjustment of large scale air-sea energy flux parameterizations by direct estimates of ocean heat transport. J. Clim. 2, 1173–1184.

Large, W. C., McWilliams, J. C., Doney, S. C., 1994. Oceanic vertical mixing: A review and a model with a nonlocal boundary layer parametrization. Rev. Geophys. 32 (4), 363–403.

Lipscomb, W., 2001. Remapping the thickness distribution in sea ice models. J. Geophys. Res. 106 (C7).

Maykut, G. A., 1982. Large-scale heat exchange and ice production in the central Arctic. J. Geophys. Res. 87 (C10), 7971–7984.

Maykut, G. A., Untersteiner, N., 1971. Some results from a time-dependent thermodynamic model of sea ice. J. Geophys. Res. 76 (6), 1550–1575.

Mellor, G. L., Kantha, L., 1989. An ice-ocean coupled model. J. Geophys. Res. 1989, 10937–10954.

Nilsen, J., Gao, Y., Drange, H., Furevik, T., Bentsen, M., 2003. Simulated North Atlantic-Nordic Seas water mass exchanges in an isopycnic coordinate OGCM. Geophys. Res. Lett. 30 (10), 1536, doi:10.1029/2002GL016597.

Østerhus, S., Turrell, W. R., Jónsson, S., Hansen, B., apr 2005. Measured volume, heat, and salt fluxes from the Atlantic to the Arctic Mediterranean. Geophys. Res. Lett. 32 (7), L07603, doi:10.1029/2004GL022188.

Payne, R. E., 1972. Albedo of the sea surface. J. Atmos. Sci. 29, 959–970.

Roeckner, E., Arpe, K., Bengtsson, L., Brinkop, S., Dümenil, L., Esch, M., Kirk, E., Lunkeit, F., M. Ponater, B. R., Sausen, R., Schlese, U., Schubert, S., Windelbrand, M., 1992. Simulation of the present-day climate with the ECHAM model: Impact of model physics and resolution. Tech. Rep. 93, Max-Plank Institut für Meteorologie, Hamburg.

Rothrock, D. A., Zhang, J., Yu, Y., 2003. The arctic ice thickness anomaly of the 1990s: A consistent view from observations and models. J. Geophys. Res. 108 (C3), 3083, doi:10.1029/2001JC001208.

Salas Mélia, D., 2002. A global coupled sea ice–ocean model. Ocean Modelling 4 (2), 137–172.

Schramm, J., Holland, M., Curry, J., Ebert, E., 1997. Modeling the thermodynamics of a sea ice thickness distribution. 1. Sensitivity to ice thickness resolution. J. Geophys. Res. 102, 23–23.

Semtner Jr., A. J., 1976. A model for the thermodynamic growth of sea ice in numerical investigations of climate. J. Phys. Oceanogr. 6 (3), 379–389.

Steele, M., 1992. Sea ice melting and floe geometry in a simple ice-ocean model. J. Geophys. Res. 97, 17729–17738.

Sun, S., Bleck, R., Rooth, C. G. H., Dukowicz, J., Chassignet, E. P., Killworth, P., 1999. Inclusion of thermobaricity in isopycnic-coordinate ocean models. J. Phys. Oceanogr. 29, 2719–2729.

Svendsen, E., Kloster, K., Farrelly, B., Johannessen, O. M., Johannessen, J. A., Campbell, W. J., Gloersen, P., Cavalieri, D., Mätzler, C., 1983. Norwegian remote sensing experiment: Evaluation of the nimbus 7 scanning multichannel microwave radiometer for sea ice research. J. Geophys. Res. 88 (C5), 2781–2791.

Teague, W., M.J., C., P.J., H., 1990. A comparision between the Generalized Digital Environmental Model and Levitus climatologies. J. Geophys. Res. 95 (C5), 7167–7183.

Thorndike, A. S., Rothrock, D. A., Maykut, G. A., Colony, R., 1975. The thickness distribution of sea ice. J. Geophys. Res. 80 (33), 4501–4513.

Vinje, T., Nordlund, N., Kvambekk, Å., 1998. Monitoring ice thickness in Fram Strait. J. Geophys. Res. 103 (C5), 10437–10449.

Woodgate, R. A., Aagaard, K., Weingartner, T. J., 2005. Monthly temperature, salinity, and transport variability of the Bering Strait through flow. Geophys. Res. Lett. 32, L04601, doi:10.1029/2004GL021880.